JM PAPERS

Transition to turbulence on a rotating wind turbine blade at $Re_c = 3 \times 10^5$

T.C.L. Fava[1],[†], **D. Massaro**[1], **P. Schlatter**[1,2], **D.S. Henningson**[1] and **A. Hanifi**[1]

[1]FLOW, Department of Engineering Mechanics, KTH Royal Institute of Technology,
SE-100 44 Stockholm, Sweden

[2]Institute of Fluid Mechanics, Friedrich–Alexander–Universität Erlangen–Nürnberg, 91058 Erlangen,
Germany

The boundary-layer stability on a section of a rotating wind turbine blade with an FFA-W3 series aerofoil at a chord Reynolds number of 3×10^5, with varying rotation and radii, is studied with direct numerical simulations and linear stability analyses. Low rotation does not significantly affect transition in the outboard blade region. The relative insensitivity to rotation is due to a laminar separation bubble near the leading edge, spanwise-deformed by a primary self-excited instability, promoting the secondary absolute instability of the Kelvin–Helmholtz (KH) vortices and rapid transition. Moderate increases in rotation, or moving inboard, stabilise the flow by accelerating the attached boundary layer and possibly inducing competition between cross-flow and KH modes. This delays separation and transition. Initially, for high rotation rates or radial locations close to the hub, transition is delayed. Nevertheless, strong stationary and travelling cross-flow modes are eventually triggered, spanwise modulating the KH rolls and shifting the transition line close to the leading edge. Cross-flow velocities as high as 56 % of the free stream velocity directed towards the blade tip are reached at the transition location. For radial locations farther from the hub, the effective angle of attack is decreased, and cross-flow transition occurs at lower rotation rates. The advance or delay of the transition line compared with a non-rotating configuration depends on the competing rotation effects of stabilising the attached boundary layer and triggering cross-flow modes in the separation flow region.

Key words: boundary layer stability, transition to turbulence, absolute/convective instability

1. Introduction

System rotation may engender various types of flow instabilities, as demonstrated for channel flows subject to spanwise rotation (Hart 1971; Lezius & Johnston 1976), in which regularly spaced stationary streamwise vortices appear at a lower Reynolds number than

† Email address for correspondence: fava@kth.se

Tollmien–Schlichting (TS) waves (Tritton & Davies 1985; Alfredsson & Persson 1989). Transition to turbulence occurs through the secondary instability of these vortices, characterised by their twisting (Alfredsson & Persson 1989; Wall & Nagata 2006). Experiments indicate that cyclonic rotation (parallel to mean vorticity/shear) is stabilising, whereas anticyclonic rotation (antiparallel to mean vorticity/shear) is destabilising (Koyama *et al.* 1979). This effect also occurs in Blasius (Potter & Chawla 1971; Dechamps & Hein 2018) and turbulent (Tritton 1992) boundary layers. The stabilisation engendered by cyclonic rotation reduces the receptivity to free stream disturbances (Masuda & Matsubara 1990) and changes the optimal perturbation from streamwise vortices (low rotation) to spanwise vortices (high rotation) (Yecko & Rossi 2004).

More relevant to wind turbine applications are the configurations in which the rotation axis is orthogonal to the spanwise direction. The generated cross-flow profiles may be prone to inflectional (cross-flow) instability (Saric, Reed & White 2003). The rotating disk (von Kármán 1921) epitomises such flow configuration, where cross-flow vortices form an angle of $14°$ to the radius (Gregory, Stuart & Walker 1955). Stability analyses by Malik (1986) allowed obtaining the neutral curve for stationary disturbances. Balachandar, Streett & Malik (1992) showed a primary disturbance root mean square (r.m.s.) amplitude of 9% of the disk rotation speed for the inception of secondary instability, characterised by counter-rotating vortices superimposed on the cross-flow structures. Short-wavelength vortices are more susceptible to secondary instability but not the most amplified primary disturbances. The presence of axial flow reduces the amplification of the cross-flow instability as the cross-flow profiles become less inflectional (Garrett, Hussain & Stephen 2010), which may explain the irrelevance of cross-flow modes to transition in the wind turbine blade study of Jing, Ducoin & Braud (2020). The rotating disk flow is convectively stable in the circumferential direction but absolutely unstable in the radial direction above a critical radius-based Reynolds number (Lingwood 1995, 1996), explaining the insensitivity of transition to the disturbance level (Malik, Wilkinson & Orszag 1981). The marine propeller investigated by Jing & Ducoin (2020) displayed similar instability mechanisms to the rotating disk.

Regarding fan blades, cross-flow modes driven by rotation seem too weak to trigger transition (Pascal *et al.* 2020; Theiss *et al.* 2022), even though their growth rates tend to increase with the rotation rate (Dechamps & Hein 2018). Likewise, experiments showed that transition on a rotating helicopter blade occurred via two-dimensional TS waves, with rotation not affecting the transition location (Weiss *et al.* 2017, 2019, 2020). This may be due to the attached character of the flow, where Coriolis and centrifugal forces are in balance, and there is a low cross-flow (McCroskey 1971). Other experiments on rotating aeronautical propellers showed that the flow transitioned to turbulence over a laminar separation bubble (LSB), whose starting point shifted abruptly to the leading edge above a critical radius (Schülein, Rosemann & Schaber 2012; Lang *et al.* 2015). The role of rotation and spanwise flow in this mechanism is unclear. Toppings & Yarusevych (2023) observed an increased spanwise velocity inside LSBs near a stationary wing tip and root, triggering modes travelling in the same direction as this flow. In the case of a swept LSB, the literature suggests that a self-excited LSB instability is little affected by the cross-flow (Hosseinverdi & Fasel 2016).

In the few detailed numerical simulations regarding the stability of rotating wind turbine blades, rotation-induced cross-flow instability was observed in some cases (Gross *et al.* 2012; Fava, Henningson & Hanifi 2024) but not noted in Jing *et al.* (2020). The linear stability analysis of the flow on a wind turbine blade obtained from the boundary layer equations showed a partial stabilisation of TS waves by rotation (Hernandez 2012).

There was no mention of cross-flow modes. Thus, the role of cross-flow instability in transition seems highly dependent on the blade geometry and operating condition. The cross-flow on wind turbine blades scales with the solidity ($s = c^*/r^*$), where c is the chord length, r is the radial position and $*$ denotes dimensional variable (Shen & Sørensen 1999; Chaviaropoulos & Hansen 2000). Dumitrescu & Cardos (2004) showed, solving the boundary layer equations for a rotating flat plate, that the outward radial flow scales with Ro_r^{-2}, where $Ro_r = \Omega^* r^*/U_\infty^*$, and Ω and U_∞ are the angular and relative inflow velocities. This phenomenon, denominated centrifugal pumping (McCroskey & Yaggy 1968), is due to an imbalance between centrifugal and Coriolis forces upon flow separation (Corten 2001). Measurements indicated nearly radial flow in the laminar separated flow on fan (Schülein *et al.* 2012; Pascal *et al.* 2020) and wind turbine (Savino & Nyland 1985; Schreck & Robinson 2002; Schreck, Sørensen & Robinson 2007) blades. There may be secondary effects of that, such as the creation of a favourable pressure gradient delaying separation and transition (McCroskey & Yaggy 1968; Du & Selig 2000; Dumitrescu & Cardos 2004) although such effects are not a consensus (Bosschers 1995; Sicot *et al.* 2008). From the above, it is clear that low Ro_r or high s is conducive to increased cross-flow effects (Shen & Sørensen 1999; Dumitrescu & Cardos 2012; Fava *et al.* 2021). Unfortunately, transition experiments involving wind turbine blades display limited spatial resolution of the transition process, besides being focused on the outboard blade region (high Ro_r) (Schaffarczyk, Schwab & Breuer 2017; Dollinger *et al.* 2018; Reichstein *et al.* 2019).

The impact of rotation on transition is largely unexplored or subject to debate, yet comprehending these effects is crucial for improving transition prediction and rotor performance (Schülein *et al.* 2012; Lang *et al.* 2015; Dechamps & Hein 2018; Jaroslawski *et al.* 2022). Despite the available works, experimental details on the transition process are lacking due to difficulties in acquiring data in rotating frames. Moreover, high-fidelity simulations of these configurations, which could overcome these difficulties, are scarce. Therefore, the present work attempts to bridge this gap with direct numerical simulations of a rotating wind turbine blade section at $Re_c = 3 \times 10^5$. This value is in the range of small horizontal axis wind turbines (Karthikeyan *et al.* 2015), whereas large rotors typically display $Re_c = 3 \times 10^6$–1.5×10^7 (Jung *et al.* 2022). The rotation numbers $Ro_c = \Omega^* c^*/U_\infty^*$ and $Ro_r = \Omega^* r^*/U_\infty^*$ are varied, including the inboard blade region. The results are compared with non-rotating simulations. This article extends the investigations of Fava *et al.* (2024), performed for $Re_c = 1 \times 10^5$, fixed radial location and three angles of attack. Insights into the instability mechanisms are gained with primary and secondary linear stability theory (LST). The study aims to answer the following questions. (i) Are transition, flow separation and reattachment shifted upstream (or downstream) by rotation? (ii) Does rotation induce cross-flow instability? (iii) Are there significant topological flow changes and modifications in the transition mechanisms generated by rotation?

The paper is divided as follows. Section 2 presents the problem modelling and numerical methods. Section 3 contains the results, with the mean-flow characterisation and the assessment of the roles of the rotation rate, radial location and adverse pressure gradient (APG) on transition. The conclusions are drawn in § 4.

2. Methods

2.1. *Model problem*

The study concerns a rotating wing section with spanwise width $L_z = L_z^*/c^* = 0.25$, at $r^*/R^* = 0.68$, where L_z is the spanwise length, c is the chord length, r is the radial position

and R is the rotor radius. The asterisk, $*$, denotes dimensional variables. The aerofoil is a blend of 96 % of the FFA-W3-241 and 4 % of the FFA-W3-301 profiles (Björck 1990) used in the DTU 10-MW Reference Wind Turbine (Bak *et al.* 2012).

The simulations are in the rotating frame of reference (fixed to the blade). The Coriolis and centrifugal terms are included in the right-hand side of the momentum equation. They are given by

$$\left. \begin{aligned} f_x &= \underbrace{-2\Omega_y u_z}_{A_x} \underbrace{-\Omega_y \Omega_x y + \Omega_y^2 (x - x_0)}_{B_x}, \\ f_y &= \underbrace{+2\Omega_x u_z}_{A_y} \underbrace{+\Omega_x^2 y - \Omega_x \Omega_y (x - x_0)}_{B_y}, \\ f_z &= \underbrace{-r\Omega^2}_{C_z} \underbrace{-2\Omega_x u_y + 2\Omega_y u_x}_{A_z}, \end{aligned} \right\} \tag{2.1}$$

where $\Omega_x = \Omega \sin\phi$, $\Omega_y = \Omega \cos\phi$ and ϕ is the geometric twist angle; u_x, u_y and u_z are the velocity components in x, y and z x_0 is the streamwise location of the rotation centre along the blade; $\boldsymbol{A} = (A_x, A_y, A_z)$ is the Coriolis acceleration; $\boldsymbol{B} = (B_x, B_y, 0)$ is the centrifugal acceleration due to the difference between the local radius and the radius at x_0 (r); $\boldsymbol{C} = (0, 0, C_z)$ is the centrifugal acceleration over a circular shell with radius r. Equation (2.1) can be rewritten in vector form as $\boldsymbol{f} = (f_x, f_y, f_z)$ given by

$$\boldsymbol{f} = \underbrace{Ro_c \tilde{\boldsymbol{f}}_{Co}}_{A} + \underbrace{Ro_c^2 \tilde{\boldsymbol{f}}_{Cent_1}}_{B} + \underbrace{Ro_c Ro_r \tilde{\boldsymbol{f}}_{Cent_2}}_{C}, \tag{2.2}$$

where $Ro_c = \Omega^* c^* / U_\infty^* = \Omega$ and $Ro_r = \Omega^* r^* / U_\infty^*$ are the rotation numbers, where $U_\infty^* = \sqrt{(V_\infty^*)^2 + (\Omega^* r^*)^2}$, V_∞ and Ω are the wind and angular velocities (Gross *et al.* 2012). Note that $Ro_c Ro_r = Ro_c^2 / s$, where $s = c^* / r^* = 1/r$ is the solidity. Buckingham's Π-theorem predicts three non-dimensional parameters, considering physical variables U_∞^*, Ω^*, r^*, ρ^*, μ^* and c^*, where ρ is the density and μ is the dynamic viscosity. Some possibilities are $Re_c = \rho^* U_\infty^* c^* / \mu^*$, Ro_c, Ro_r and r (or s). We select Re_c, Ro_c and Ro_r as governing parameters. Here Ro_r is directly connected with the ratio between the rotational and wind speeds $\lambda_r = \Omega^* r^* / V_\infty^*$ by $Ro_r = 1/\sqrt{1 + \lambda_r^{-2}}$ and to the angle of attack $AoA = \arctan(\lambda_r^{-1}) - \phi$. For $r^* = R^*$, λ_r becomes the tip-speed ratio λ. Therefore, although not providing further information than Ro_r, the parameters r, s, λ_r and AoA will be provided since they present an enhanced physical intuition.

The forcing $\boldsymbol{f}$ enters the incompressible Navier–Stokes equation as follows:

$$\left. \begin{aligned} \frac{\partial \boldsymbol{u}}{\partial t} + \boldsymbol{u} \cdot \nabla \boldsymbol{u} &= -\nabla p + \frac{1}{Re_c} \nabla^2 \boldsymbol{u} + \boldsymbol{f}, \\ \nabla \cdot \boldsymbol{u} &= 0, \end{aligned} \right\} \tag{2.3}$$

where $\boldsymbol{u} = (u_x, u_y, u_z)$, p is the pressure and Re_c is the chord Reynolds number. All quantities are non-dimensionalised by the relative free stream wind velocity (U_∞^*) and chord (c^*). Figure 1 shows the domain and coordinate systems. The y' axis is orthogonal to the rotor plane (parallel to the incoming wind), and z' is the spanwise direction. Due to the twist angle ϕ, a new coordinate system x, y, z oriented along the chord, parallel to the leading edge and in the spanwise direction, respectively, is defined and used in the study.
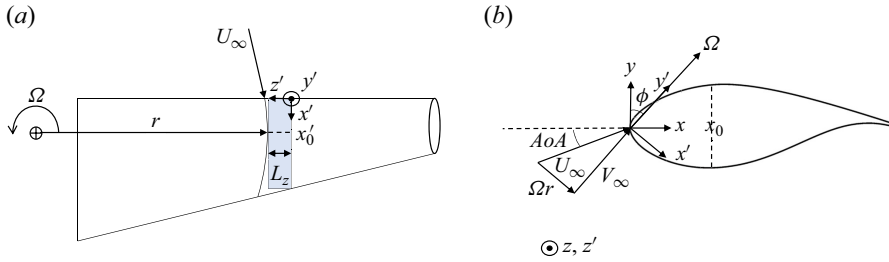
999 A54-4

Figure 1. Schematic representation of the simulation domain (blue region) and the blade section. The following symbols are used: Ω, rotation vector/rate; r, radius at point x_0; L_z, width of the simulation domain; AoA, angle of attack; ϕ, twist angle; U_∞, V_∞, Ωr, relative free stream, wind and rotation velocities.

The kinematic relations of the rotation domain in the x, y and z coordinate system, employed as boundary conditions, are given by

$$\left.\begin{aligned} u_x &= +\Omega r \cos\phi + V_\infty \sin\phi, \\ u_y &= -\Omega r \sin\phi + V_\infty \cos\phi, \\ u_z &= +\Omega[(x - x_0)\cos\phi - y\sin\phi], \end{aligned}\right\} \quad (2.4)$$

which can be rewritten in terms of the non-dimensional parameters as

$$\left.\begin{aligned} u_x &= +Ro_r \cos\phi + Ro_r/\lambda_r \sin\phi, \\ u_y &= -Ro_r \sin\phi + Ro_r/\lambda_r \cos\phi, \\ u_z &= +Ro_c[(x - x_0)\cos\phi - y\sin\phi]. \end{aligned}\right\} \quad (2.5)$$

Therefore, given a fixed geometry (including ϕ), kinematic and dynamic similarity can be achieved for the same Re_c, Ro_c and Ro_r (or AoA or λ_r). Note that the boundary conditions are imposed sufficiently far away from the airfoil, so the induced angle of attack is negligible. Moreover, no spanwise variation of the geometry, forcing and boundary conditions is assumed, since L_z/r is small.

2.2. *Numerical procedure*

The direct numerical simulation of the incompressible Navier–Stokes equations (2.3) is performed with Nek5000 (Fischer, Lottes & Kerkemeier 2008). Nek5000 is an open-source, highly scalable and portable code based on the spectral element method (Patera 1984), with minimal dissipation, high accuracy and nearly exponential convergence. The spectral element method can be viewed as a high-order version of the finite element method, where the computational domain is discretised into a finite number of non-overlapping elements. The basis functions, defined on each element, are polynomials with order N. In this study, $N = 7$ is employed (Deville, Fischer & Mund 2002). The equations are solved in weak form, using a $\mathbb{P}_N - \mathbb{P}_{N-2}$ formulation, where $\mathbb{P}_N$ is the polynomial approximation space of the velocity and $\mathbb{P}_{N-2}$ is that of the pressure. The velocity and pressure fields are expanded with Lagrange interpolants on Gauss–Lobatto–Legendre and Gauss–Legendre points. As high-order methods present very low numerical dissipation, numerical instabilities might arise. Thus, the highest wavenumbers are filtered with an implicit filter (Negi, Schlatter & Henningson 2017). The time integration is performed via third-order implicit backward differentiation, with

a third-order extrapolation scheme for the convective term. A Courant–Friedrichs–Lewy number below 0.4 is guaranteed by using a time step $\Delta t^* U_\infty / c = 5 \times 10^{-6}$.

Adaptive mesh refinement is used to design a non-conforming mesh that reduces the influence of boundary conditions on the aerofoil, by increasing the computational domain, and lowers computational cost. The adaptive mesh refinement was implemented in Nek5000 (Offermans 2019; Massaro, Peplinski & Schlatter 2023*d*) and extensively used in turbulent (Peplinski *et al.* 2020; Massaro, Peplinski & Schlatter 2023*b,c*; Offermans *et al.* 2023; Toosi *et al.* 2023) and transitional (Massaro *et al.* 2023*a*; Massaro & Schlatter 2024) flows. The isotropic *h*-refinement is based on the interpolation and quadrature errors measured by the spectral error indicator (Mavriplis 1989). The mesh design process ends when the final non-conforming mesh (adapted for each case) is frozen. Then we start to collect data on the final mesh (Massaro *et al.* 2024). Further details can be found in Offermans (2019) and Massaro (2024). The wall resolution is evaluated with the largest distance between two Gauss–Lobatto–Legendre points normalised by the viscous length scale (l^*). The mean values respect $\Delta x^+ \leq 8.4$, $\Delta y^+ \leq 1.3$, $\Delta z^+ \leq 4.0$ on the suction side and $\Delta x^+ \leq 20.0$, $\Delta y^+ \leq 0.5$, $\Delta z^+ \leq 5.1$ on the pressure side, where $^+$ indicates normalisation by l^*.

The computational domain extends in the horizontal, vertical and spanwise directions from $x = -20$ to $x = 20$, $y = -20$ to $y = 20$ and $z = 0$ to $z = 0.25$ (coordinates in figure 1). The computational domain is enlarged 2.5 times in the spanwise direction and 13 times in the x and y ones compared with Fava *et al.* (2024). The aerofoil extends from $x = 0$ to $x = 1$. A Dirichlet velocity boundary condition (2.4) is imposed at the inflow at $x = -20$. A Neumann boundary condition of the form $(-p\boldsymbol{I} + 1/Re_c \nabla \boldsymbol{u}) \cdot \boldsymbol{n} = 0$, where $\boldsymbol{I}$ is the identity matrix and $\boldsymbol{n}$ is the outward normal unitary vector, is applied to the outlet face at $x = 20$. Finally, periodic boundary conditions are applied in the spanwise direction ($z = 0$ and $z = 0.25$). To avoid any dependency of transition on the (minimal) numerical noise, a tripping forcing technique (Schlatter & Örlü 2012) is used in the free stream flow, positioned 5 % of the chord length upstream of the blade leading edge ($x = -0.05$). The forcing term is a weak stochastic volume force acting on the right-hand side of the momentum equation, and it is given by

$$\left. \begin{aligned} F &= f(z, t) \exp\left[\frac{(x - x_0)^2}{l_x^2} - \frac{y^2}{l_y^2} \right], \\ f(z, t) &= T_s g(z) + T_u \{ [1 - b(t)] h^i(z) + b(t) h^{i+1}(z) \}. \end{aligned} \right\} \tag{2.6}$$

The function $f(z, t)$ consists of two terms, corresponding to steady and unsteady perturbations, with amplitudes T_s and T_u, respectively; l_x and l_y are the spatial Gaussian attenuation of the forcing region in x and y, $b(t) = 3p^2 - 2p^3$, $p = t/t_s - i$, $i = \text{int}(t/t_s)$; $g(z)$ and $h^i(z)$ are Fourier series with unit amplitude for all wavenumbers below $2\pi/l_z$ and zero amplitude otherwise. The parameters are chosen as $l_x = 1.8 \times 10^{-3}$, $l_y = 4.6 \times 10^{-4}$, $l_z = 7.8 \times 10^{-4}$, $T_s = 0$, $T_u = 1 \times 10^{-6}$ and $t_s = 7.9 \times 10^{-4}$. Section 3.2.2 assesses the impact of the introduced noise on the instability mechanisms.

Several cases with varying Ro_r (*AoA* or λ_r) and Ro_c for fixed $Re_c = 3 \times 10^5$ are studied. The geometric twist angle $\phi = 4.8°$ is kept constant. Table 1 summarises the main parameters employed in the simulations. The non-rotating cases (4B and 5B) are obtained by considering $\boldsymbol{f} = \boldsymbol{0}$ in (2.3) (no Coriolis and centrifugal effects), and the same boundary

Case	r	s	AoA (°)	λ_r	Ro_r	Ro_c ($\equiv \Omega$)	Status
4A	18.2	0.0549	12.8	3.1487	0.9531	0.0523	Rotating
4B	18.2	0.0549	12.8	0	0	0	Non-rotating
4C	6.08	0.1645	12.8	3.1487	0.9531	0.1570	Rotating
4D	3.04	0.3289	12.8	3.1487	0.9531	0.3140	Rotating
5A	6.08	0.1645	4.2	6.2975	0.9876	0.1627	Rotating
5B	6.08	0.1645	4.2	0	0	0	Non-rotating

Table 1. Parameters of the studied cases. The following definitions are made: $r = r^*/c$, non-dimensional radial location; $s = c/r^*$, solidity; AoA, angle of attack; $\lambda_r = \Omega^* r^*/V_\infty$; $Ro_r = \Omega^* r^*/U_\infty$; $Ro_c = \Omega^* c/U_\infty = \Omega$.

conditions (see (2.5)) as their rotating counterparts (cases 4A and 5A), but setting $u_z = 0$. Note that cases within the same group (4A–4D, 5A and 5B) share the same AoA.

3. Results

The results presented in the following sections concern the suction side of the blade, as it is the most crucial in terms of transition. In the remainder of the manuscript, the quantities are non-dimensionalised with the relative free stream velocity (U_∞^*) and chord length (c^*) or derivative quantities if not otherwise indicated. Furthermore, y will indicate the wall-normal coordinate.

3.1. *Outline of mean results*

Figure 2 compares the spanwise- and time-averaged pressure distributions. The pressure progressively decreases in the second half of the chord on the suction side with the rotation rate for cases 4B, 4A, 4C and 4D. On the pressure side, the only significant difference occurs in case 4D, presenting a higher pressure than its lower rotation counterparts. The improved lift of case 4D may be associated with cross-flow transition (see § 3.3), suggesting that this phenomenon may be a path for rotational augmentation (Himmelskamp 1947), as also highlighted by Gross *et al.* (2012). Cases 5A and 5B present a significantly reduced APG on the suction side due to a higher Ro_r and lower angle of attack ($AoA = 4.2°$). However, unlike the four-series cases, the pressure difference and, consequently, the lift is lower for the rotating blade (case 5A) compared with the non-rotating blade (case 5B).

Table 2 summarises the spanwise- and time-averaged quantities related to the transition process. In case 4D, the time series consists of two windows, before and after the occurrence of cross-flow transition at time T_b. The split is necessary as the flow switches at T_b, changing significantly. x_{b_1}, x_{b_2} and $x_{h_{max}}$ denote the streamwise locations of separation, reattachment and maximum height of the LSB. The LSB edge is defined as the zero streamwise mass-flux line, i.e. (x, y_b) fulfilling $\int_0^{y_b} \langle U \rangle_{z,t}(x, \xi) \, \mathrm{d}\xi = 0$, where y_b is the LSB height and $\langle U \rangle_{z,t}$ is the spanwise- and time-averaged streamwise velocity (Avanci, Rodríguez & Alves 2019). Thus, $h_{max} = \max_x y_b$ is the maximum LSB height, and h_{max}/δ^* is this quantity scaled with the local displacement thickness (δ^*). Here $x_{u_{r,max}}$ and $u_{r,max}$ correspond to the streamwise location of the maximum reverse flow and the value of the latter, respectively; $u_{cr_{tr}}$ is the cross-flow velocity inside the boundary layer at the transition location x_{tr}, the latter defined as the streamwise location of maximum boundary layer shape factor $H = \delta^*/\theta$ (Jaroslawski *et al.* 2023); θ is the momentum thickness.
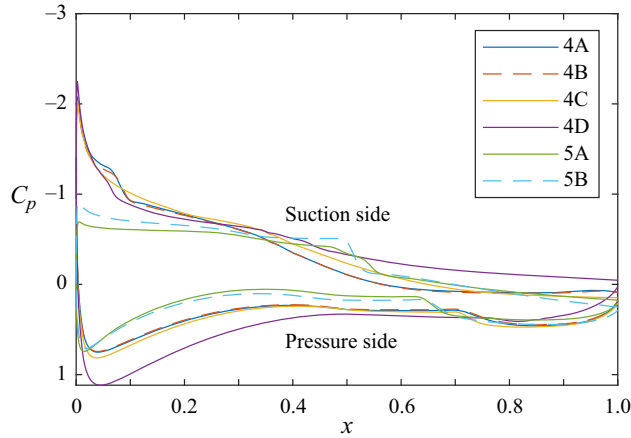
Figure 2. Spanwise- and time-averaged pressure distributions.

Case	Window	x_{b_1}	x_{b_2}	$x_{h_{max}}$	$h_{max} \times 10^3$	h_{max}/δ^*	$x_{u_{r,max}}$	$u_{r,max}$	$u_{cr_{tr}}$	x_{tr}
4A	—	0.017	0.082	0.061	1.513	0.687	0.064	−0.126	−0.048	0.061
4B	—	0.018	0.088	0.066	1.454	0.661	0.069	−0.118	0	0.066
4C	—	0.033	0.113	0.079	0.447	0.269	0.073	−0.011	−0.216	0.073
4D	$T < T_b$	0.348	0.484	0.452	3.837	0.679	0.455	−0.107	−0.283	0.448
	$T > T_b$	0.013	0.031	0.024	0.244	0.224	0.020	−0.010	−0.561	0.020
5A	—	0.350	0.558	0.488	6.718	0.772	0.536	−0.067	−0.116	0.479
5B	—	0.328	0.523	0.479	7.571	0.821	0.502	−0.206	0	0.467

Table 2. Spanwise- and time-averaged transition-related quantities. The following definitions are used: x_{b_1}, x_{b_2} and $x_{h_{max}}$, separation, reattachment and LSB maximum height locations; h_{max} and δ^*, maximum LSB height and local displacement thickness; $x_{u_{r,max}}$ and x_{tr}, maximum reverse flow and transition locations; $u_{r,max}$, maximum reverse velocity; $u_{cr_{tr}}$, cross-flow velocity at x_{tr}.

3.2. Outboard blade region: null and low rotation speed

3.2.1. Flow characteristics

Case 4A corresponds to the outboard blade region (high radial position) and low rotation speed, whereas case 4B is its non-rotating counterpart. Figures 3(*a*) and 3(*b*) display the isosurfaces of $\lambda_2 = -100$ (normalised by U_∞^2/c^2) coloured by the instantaneous streamwise velocity. Two-dimensional spanwise rolls form near the leading edge, characteristic of a Kelvin–Helmholtz (KH) instability due to the inflectional velocity profiles in a flow separation region (Dovgal, Kozlov & Michalke 1994; Brinkerhoff & Yaras 2011; Boutilier & Yarusevych 2012). The rolls correspond to the nonlinear growth phase of the instability near the location of maximum separation height (Toppings & Yarusevych 2023). The central frequency of the unstable region of KH modes typically determines the mean vortex shedding frequency (f_s) (Kirk & Yarusevych 2017), which lies in the range $f_s\theta_s/u_s = 0.005$–0.016, where θ_s and u_s are the momentum thickness and edge velocity at the separation point (Pauley, Moin & Reynolds 1990; Brinkerhoff & Yaras 2011). Cases 4A and 4B present $f_s\theta_s/u_s = 0.011$–0.012 ($f_s = 84.7$), in agreement with the frequency of KH modes in the literature.

The λ_2 isosurfaces indicate two turbulence wedges fixed at given spanwise locations (independent of the numerical noise parameters), where the KH rolls and turbulence spots
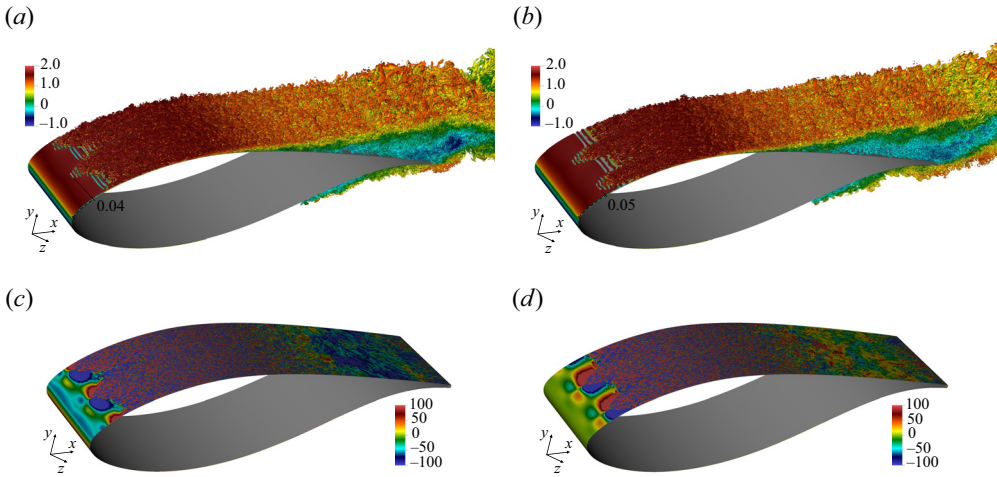
Figure 3. The λ_2-structures ($\lambda_2 = -100$) coloured by the streamwise velocity (a,b) and isocontours of streamwise vorticity (ω_x) on a near-wall plane (c,d) for cases 4A (a,c) and 4B (b,d).

appear earlier. These wedges and the transition location start slightly more upstream in the rotating case (table 2). The appearance of the wedges in both cases demonstrates that they are unrelated to rotation. The isocontours of instantaneous streamwise vorticity (ω_x) on a near-wall plane, in figures 3(c) and 3(d), provide further insight into the wedge structure. The spanwise flow in the $-z$ direction in the rotating case creates $\omega_x < 0$ upstream of the wedges, whereas $\omega_x = 0$ in the non-rotating case. Two pairs of opposite-sign vorticity regions occur where the turbulence wedges are located. There is a fast turbulent breakdown to small-scale turbulence in the region where vorticity changes sign inside these two pairs.

Figure 4 presents the ω_x contours on a cross-section passing through these cells at $x = 0.05$. In case 4B, there are three lobes in the vertical direction, located in $y \approx 0 - y_r$, $y \approx y_r - y_{i_1}$ and $y \approx y_{i_1} - y_m$, where y_r (dash–dotted line), y_{i_1} (dashed line) and y_m (dotted line) are the locations of the zero streamwise velocity, inflection point and maximum streamwise velocity, respectively. The peak amplitude of the intermediate lobe agrees with the zero streamwise mass-flux line (y_b, solid line). The structure resembles the eigenmode obtained with the linear stability analysis on the yz plane of an LSB (Rodríguez, Gennaro & Souza 2021). However, the latter found the varicose (symmetric) KH mode to be more unstable, whereas a sinuous KH mode, antisymmetric around the shear-layer crests, appears here. Furthermore, the most external lobe was not observed in Rodríguez *et al.* (2021), possibly due to the accelerating boundary layer in the current simulations, with peak velocity at y_m. Secondary instabilities occur and vorticity oscillations appear in the outer lobe, as shown in figure 4(b). Interestingly, streaks present a similar destabilisation mechanism where high-frequency free stream noise excites secondary instabilities in the outer region of the boundary layer (Brandt, Schlatter & Henningson 2004; Zaki & Durbin 2005). This noise cannot penetrate deeper into the boundary layer due to shear sheltering (Hunt & Carruthers 1990). In case 4A, the lobes are not centred around the shear layer crests but rather shifted to lower z besides presenting stronger vorticity. The mode is still sinuous, antisymmetric around the shifted spanwise locations and destabilisation occurs over the external lobes

Figure 5 shows a top view of the time-averaged streamwise ($\langle U \rangle_t$) and spanwise ($\langle W \rangle_t$) velocities on a wall-parallel plane at $y = 1 \times 10^{-3}$ ($y^*/h_{max} = 0.67$ or $y^*/\delta^* = 0.45$ at $x_{h_{max}}$). The mean streamwise velocity indicates that the LSB (dark blue region) features
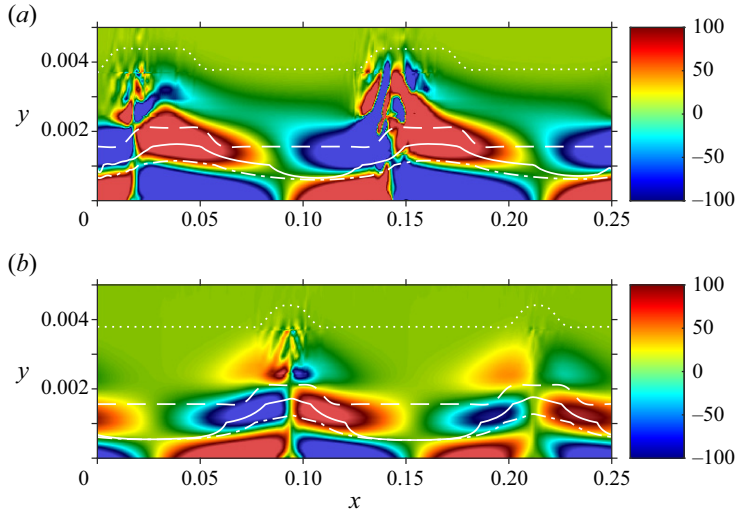
Figure 4. Isocontours of streamwise vorticity on a cross-sectional plane at $x = 0.05$ for cases 4A (*a*) and 4B (*b*). The dash–dotted line represents the end of the mean reverse flow region (y_r), the solid line depicts the mean streamwise zero mass-flux line (y_b), the dashed line is the mean normal location of the inflection point closest to the wall (y_{i_1}) and the dotted line denotes the mean maximum streamwise velocity locus (y_m).
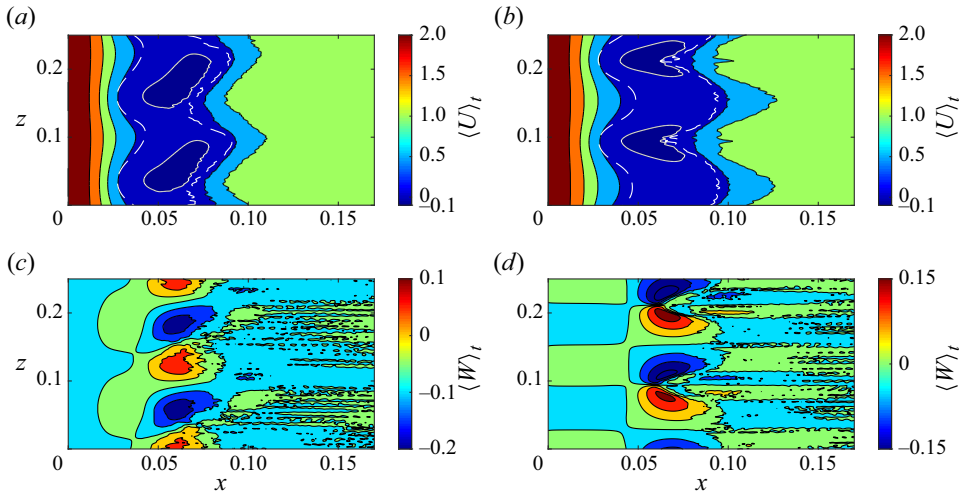

Figure 5. Contours of time-averaged streamwise (*a*,*b*) and spanwise (*c*,*d*) velocities on a plane parallel to the wall at $y = 0.001$ for cases 4A (*a*,*c*) and 4B (*b*,*d*). The solid and dashed white isolines indicate the reverse flow region at $y = 0.001$ and the first node above the wall.

a steady spanwise modulation with two wavelengths. The spanwise locations of more premature separation match those where the turbulence wedges develop in figure 3. Moreover, the regions with higher reverse flow (darkest shade of blue) are antisymmetric about a longitudinal (*xy*) plane in the rotating case and symmetric around it in the non-rotating case. The difference may arise from the preferential amplification of modes with spanwise wavenumbers (β) of the same sign as the spanwise flow (Toppings & Yarusevych 2023). Symmetry around $\beta = 0$ occurs in the non-rotating case since there is no preferential growth direction. The mean spanwise velocity indicates the same cells
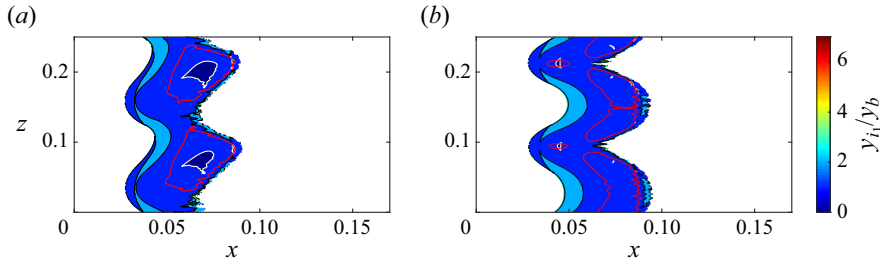
Figure 6. Contours of the ratio between the time-averaged normal location of the streamwise velocity profile inflection point (y_{i_1}) and the local height of the separation bubble (y_b) for cases 4A (*a*) and 4B (*b*). The white isoline indicates $y_{i_1}/y_b = 1$, and the red isoline denotes reverse flow $u_r = -0.12$.

as the streamwise vorticity. Rotation generates a spanwise flow of -8% at the leading edge. The extrema of $\langle W \rangle_t$ reaches -19.9% to $+9.9\%$ inside the cell in the rotating case, whereas this value spans $\pm 19.1\%$ in the non-rotating case. The lower spanwise velocity in the rotating case is due to the tip flow on top of which the cellular pattern develops.

The spanwise modulation of the LSB may have two roots (Rodríguez & Theofilis 2010). The first is a primary absolute instability (Huerre & Monkewitz 1990) of the LSB for minimum reverse flows of 12 %–25 % of the free stream velocity (Hammond & Redekopp 1998; Alam & Sandham 2000; Rist & Maucher 2002; Fasel & Postl 2004; Diwan & Ramesh 2009; Rodríguez, Gennaro & Juniper 2013). Even though the time-averaged reverse flow before three-dimensionalisation is -15.7% and -11.8% in the rotating and non-rotating cases, respectively, the inflection point in the streamwise velocity profiles is not under the zero streamwise mass-flux line, necessary for absolute instability (Avanci *et al.* 2019). The second possible mechanism is a self-excited centrifugal instability for minimum reverse flows of $\approx 7\%$ (Rodríguez & Theofilis 2010; Rodríguez *et al.* 2013). As demonstrated by Theofilis, Hein & Dallmann (2000), this leads to a stationary, three-dimensional global mode in the LSB. The new three-dimensional base flow destabilises further convective KH modes (Rodríguez *et al.* 2021; Fava *et al.* 2023a); the relative phases of the wave are spanwise distorted, inducing oblique modes whose maxima occur over regions with the highest reverse flow (Rodríguez & Gennaro 2019). This agrees with the breakdown occurring over these regions in the current simulations. Furthermore, the excitation of oblique waves can trigger the oblique instability mechanism, known to lead to a rapid breakdown to small-scale turbulence (Rist & Maucher 2002; Fava *et al.* 2024).

The three-dimensionalisation induced by the centrifugal global mode may create strong enough reverse flow pockets to trigger an absolute secondary instability (Rodríguez *et al.* 2021). The time-averaged maximum reverse flow in figure 5 reaches -22.3% near the wall at $x = 0.078$, $y = 5.1 \times 10^{-4}$, $z = 0.211$ in case 4A, and -19.0% at $x = 0.072$, $y = 5.1 \times 10^{-4}$, $z = 0.192$ in case 4B. These values are well above their spanwise- and time-averaged counterparts of -11.0% and -10.5%, respectively (table 2). A possible secondary absolute instability of the KH rolls is assessed in figure 6, which shows the contours of the ratio between the normal location of the wall-nearest inflection point (y_{i_1}) and the zero streamwise mass-flux height (y_b). The white isoline corresponds to $y_{i_1}/y_b = 1$, inside which a necessary condition for absolute instability ($y_{i_1}/y_b < 1$) is met (Avanci *et al.* 2019). The red isoline marks the reverse flow of -12%, deemed also a required condition for this phenomenon. In case 4A, these two areas overlap close to the LSB trailing edge in a way that is oblique to the streamwise direction. In case 4B, these
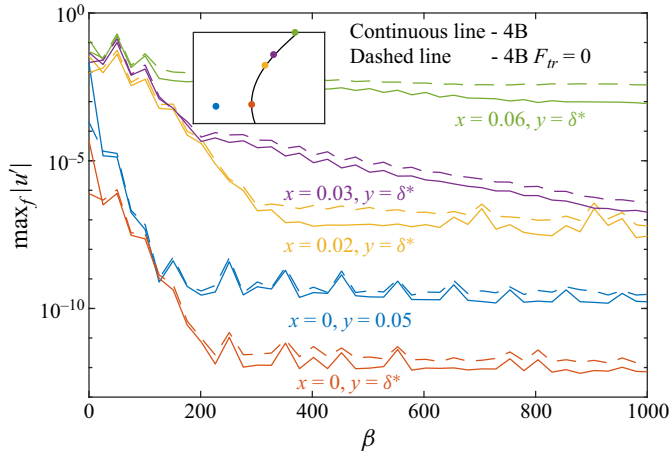
Figure 7. Spectra of streamwise velocity perturbations (maximum $|u'|$ over f) near the leading edge of the aerofoil for cases with (4B) and without (4B-$F_{tr} = 0$) introduced noise. The inset indicates the relative locations of the probes.

regions share a much smaller overlap, closer to the LSB leading edge in spanwise locations with earlier separation. In both cases, the turbulent spots nucleate close to the overlap region. Therefore, it is likely that an absolute secondary instability of the KH rolls due to the spanwise deformation of the separation bubble by a primary self-excited centrifugal instability is responsible for triggering transition.

3.2.2. *Receptivity and sensitivity of the results to the introduced noise*

Receptivity is analysed in the non-rotating case (case 4B) considering the streamwise velocity perturbation ($|u'|$) spectra inside ($x = 0 - 0.06$, $y = \delta^*$) and outside ($x = 0$, $y = 0.05$) the boundary layer. Note that the noise source is located at the latter location. The results for a corresponding case without introduced noise (case 4B-$F_{tr} = 0$) are shown to investigate the dependence of the boundary-layer dynamics on the excitation source. Figure 7 shows the results. Except possibly for $\beta = 0$ near the noise source, there are only small amplitude differences between cases 4B and 4B-$F_{tr} = 0$, with the general trend of the curves remaining the same. The maximum disturbance amplitude at $x = 0.02$–0.06 occurs for $\beta = 50.3$ ($\beta\delta^* = 0.08$, $n_z = L_z\beta/(2\pi) = 2$ wavelengths), related to the mode deforming the LSB. Peaks for this β and its harmonics appear at $x = 0$ inside and outside the boundary layer. This fact and the relative insensitivity to the introduced noise suggest that information about the three-dimensionalisation of the flow propagates upstream, supporting the claim of a self-excited instability mechanism (Huerre & Monkewitz 1990; Theofilis *et al.* 2000; Jing & Ducoin 2020).

3.2.3. *Spectral and stability analyses*

To assess the spanwise variation in the stability characteristics, computations with spatial local LST based on the linearised Navier–Stokes equations considering rotation effects are performed over several spanwise slices of the time-averaged flow. Further details can be found in Appendix A. The frequency and spanwise-wavenumber envelope of growth rates for cases 4A and 4B is shown in figure 8(*a*). The modes become unstable upon separation, clearly suggesting the role of the separated shear layer in their appearance. The growth rates are higher over the planes $z = 0.05$ and $z = 0.15$ in the rotating case and $z = 0.1$ and
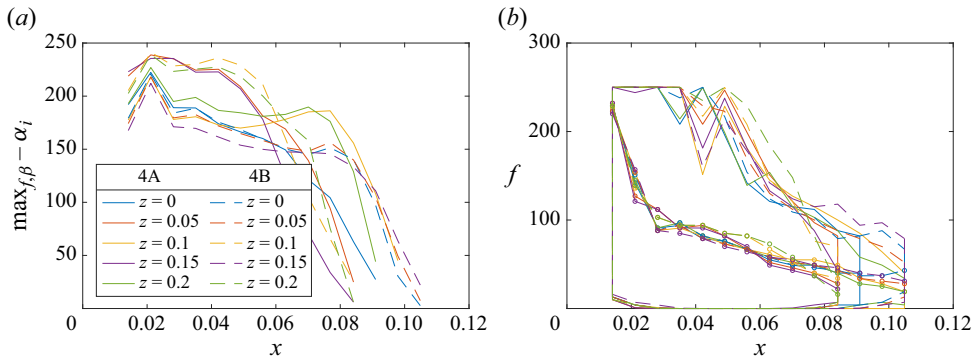
999 A54-12

Figure 8. (*a*) Growth rate (maximum over f and β) and (*b*) neutral curve (maximum over β) from local LST for several spanwise slices of the time-averaged flow of cases 4A and 4B. The line with circles in the neutral curve indicates the most-unstable frequency.

$z = 0.2$ in the non-rotating case, agreeing with the locations of stronger reverse flow (see figure 5), as also noted in other works (Rodríguez & Gennaro 2019; Fava *et al.* 2023*a*). This helps explain the earlier formation of turbulent spots over these planes. Figure 8(*b*) shows the neutral curve as a frequency and streamwise position function (maximum over β). The most amplified frequency, marked with circles, is initially high but decays as the height of the separated shear layer increases. The frequencies over planes with higher reverse flow tend to be higher. Note that the inflectional velocity profiles allow a broad range of unstable frequencies, including quasisteady perturbations (Dovgal *et al.* 1994). This analysis assumes slow variations in *x* and *z*, which may not be valid, especially considering the spanwise direction. Thus, considering the spanwise modulation of the mean flow is necessary and the analysis will be carried out later (Saxena, Leibovich & Berkooz 1999; Kawahara *et al.* 2003; Marant & Cossu 2018; Rodríguez & Gennaro 2019; Fava *et al.* 2023*a*).

Figure 9 shows the $|u'|$ boundary-layer spectra for cases 4A and 4B. Due to the inferred symmetry, only $\beta \geq 0$ is displayed. In the rotating case, a high-amplitude region appears at $f_f \approx 87$, especially visible at $x = 0.04$–0.05, attributed to KH modes. The excitation of oblique ($\beta \neq 0$) modes for this frequency is due to the rotation-generated spanwise flow (Fava *et al.* 2024). Note that this frequency agrees with the most amplified mode predicted by LST analysis in figure 8(*b*). In the non-rotating case, KH modes appear for a wide range of frequencies but are mainly two-dimensional ($\beta = 0$). Steady modes with $\beta = \pm 50.3$ ($n_z = \pm 2$), linked to the LSB deformation, also appear in both cases. The interaction between plane KH modes $(f/f_f, n_z) = (1, 0)$ and the steady distortion of the LSB $(0, \pm 2)$ also excites oblique modes $(1, \pm 2)$, resembling the mechanism described by Marxen *et al.* (2003). This mechanism is typically attributed to the growth of oblique convective TS waves in the attached boundary layer (Brinkerhoff & Yaras 2011; Michelis, Yarusevych & Kotsonis 2018). However, here, this interaction seems to be mainly driven by the $(0, \pm 2)$ global mode and $(1, 0)$ KH mode, leading to the destabilisation of the oblique KH mode (Rodríguez & Gennaro 2019).

A two-dimensional eigenvalue problem over cross-planes (*yz*) is employed to study the secondary stability of the spanwise-deformed base flow of the LSB (Rodríguez *et al.* 2021). Since the modulation is steady, the time-averaged flow is considered as the base flow. Furthermore, since the growth rates are very high, the local approach is expected to yield similar results to non-local methods such as the plane-marching parabolised stability
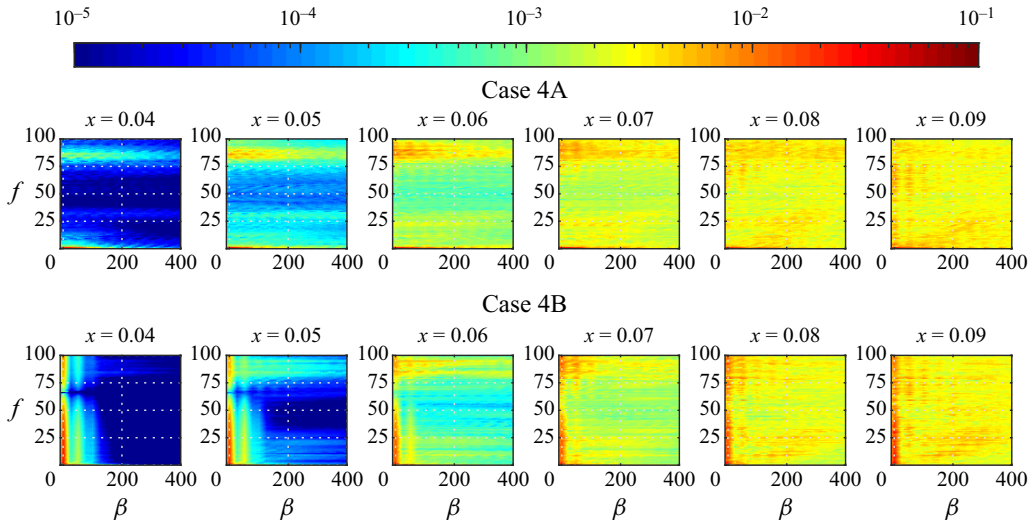
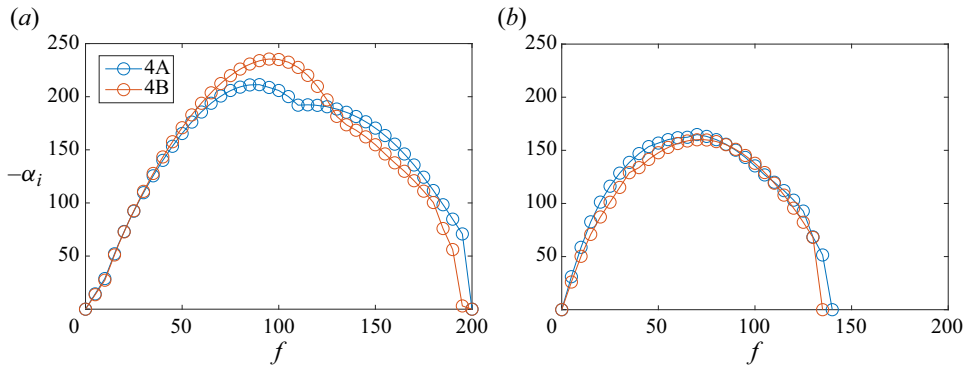Figure 9. Spectra of streamwise velocity perturbations ($|u'|$) at $y = \delta^*$ for cases 4A and 4B.

Figure 10. Growth rate from linear stability analysis over the cross-sectional planes for cases 4A and 4B for $x = 0.03$ (*a*) and $x = 0.05$ (*b*).

equations (three-dimensional parabolised stability equations) (Rodríguez & Gennaro 2019). The spatial stability problem is considered, where α^+ modes with a given frequency f are spatially amplified with growth rate $-\alpha_i$ (Schmid & Henningson 2001). Appendix B presents further details. Figure 10 shows the growth rates as a function of f. At $x = 0.03$, cases 4A and 4B display a local amplification maximum at $f = 90$–95 with phase speeds $c_p = (0.78$–$0.77)U_e$, where U_e is the local edge velocity. The maximum growth rates are higher for the non-rotating case at this location, which lies slightly downstream of separation. This may be related to the stabilising effect of rotation in the attached flow and front part of the LSB. Downstream, at $x = 0.05$, the maximum growth rate occurs at $f = 70$, with $c_p = (0.79$–$0.82)U_e$. The trend in the growth rates is reversed here, with the rotating case presenting slightly higher amplification since rotation becomes destabilising upon stronger reverse flow (Fava *et al.* 2024). The observed phase speeds are higher than those for KH rolls in an undulated shear layer ($c_p = (0.33$–$0.36)U_e$) found by Rodríguez *et al.* (2021) since the time-averaged flow here already contains the distortion introduced by the KH modes. Indeed, the phase speeds here present values close to the range of
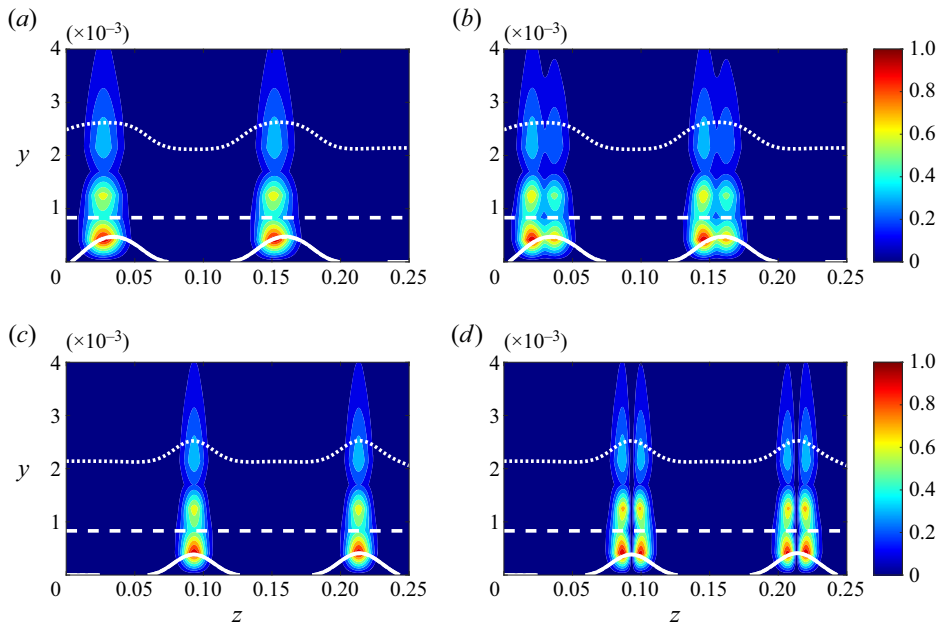
999 A54-14

Figure 11. Eigenmodes (absolute value) of the stability analysis over the cross-sectional planes at $x = 0.03$ for cases 4A (*a*,*b*) and 4B (*c*,*d*). The dash–dotted line represents the end of the mean reverse flow region (y_r), the solid line depicts the mean streamwise zero mass-flux line (y_b), the dashed line is the mean normal location of the inflection point closest to the wall (y_{i_1}) and the dotted line denotes the mean maximum streamwise velocity locus (y_m).

the varicose and sinuous secondary instability of streaks, with $c_p \approx 0.75 U_e$ (Vaughan & Zaki 2011) or $c_p = 0.87 U_e$ (Andersson *et al.* 2001). The frequencies of the most unstable modes found in the stability analysis ($f = 70$–95) agree with regions of high amplitude in the spectra of figure 9, suggesting that the secondary instability of the KH modes in the distorted shear layer is responsible for those features in the spectra.

Figure 11 shows the most amplified eigenmodes at $x = 0.03$. The reverse flow edge (dash–dotted line) and zero-streamwise mass flux line (solid line) nearly coincide since separation is weak. Furthermore, the inflection point line (dashed line) is not spanwise-deformed. The normal shear is higher than the spanwise one, and the most unstable mode (first mode) is a varicose instability, partially symmetric around the shear layer crests in case 4A and fully symmetric around them in case 4B (Swearingen & Blackwelder 1987; Brandt *et al.* 2004), as shown in figures 11(*a*) and 11(*c*). The maximum amplitude occurs over the LSB edge (solid line), lying on top of the LSB maximum height in the non-rotating case and shifted to lower z by the spanwise flow in the rotating case. A second high-amplitude region appears above the inflection point line, and a third lobe arises close to the maximum streamwise velocity line (dotted line). The mode structure resembles that of the secondary instability of KH rolls in a streaky base flow (Fava *et al.* 2023*a*). The second most unstable mode (figures 11*b* and 11*d*) is of the sinuous type, partially antisymmetric around the shear-layer crests in case 4A and fully antisymmetric around them in case 4B. This mode relies on the spanwise shear and presents only a slightly lower growth rate than the varicose mode. Interestingly, the left side of the sinuous mode presents a higher amplitude in the rotating case and the mode is shifted to the left. In case 4B, the mode is perfectly antisymmetric around the crests.
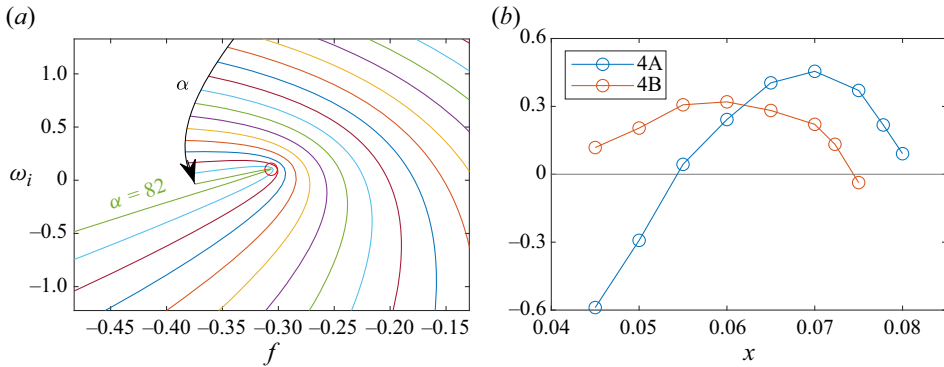
Figure 12. Absolute stability analysis over spanwise locations of maximum reverse flow ($z = 0.211$ for case 4A and $z = 0.192$ for case 4B) for $\beta = 0$. Panel (*a*) shows the cusp map for case 4B at $x = 0.0723$. The α-spacing is 1, and the cusp is represented with a red circle. Panel (*b*) shows the absolute growth rates.

The presence of absolute instability is evaluated with the cusp map (Kupfer, Bers & Ram 1987; Fava *et al.* 2024). The method is applied over spanwise slices deemed more critical according to figure 6. The growth rates are higher for $\beta = 0$, for which the results are shown. A cusp in the $\omega_i > 0$ semiplane is considered unstable. This feature is found in both cases, and the cusp is shown with a red circle in figure 12(*a*) for case 4B. It presents low frequency ($f \approx -0.3$) and growth rates, where the negative sign of f can be redefined to be positive with a change of variables involving wavenumbers in the x and z directions. The streamwise evolution of ω_i is shown in figure 12(*b*), where case 4B becomes unstable earlier, but higher growth rates are obtained in case 4A at $x = 0.07$. This is due to the destabilising rotation role inside the LSB, increasing the reverse flow. These results indicate that a secondary absolute instability of the KH rolls occurs, likely responsible for the localised breakdown to turbulence over specific spanwise locations, as seen in the simulations. Note that a finite region of absolute instability, as found here, is necessary for global instability (Huerre & Monkewitz 1990). The occurrence of an absolute secondary instability of the KH rolls, where the primary instability is the global mode responsible for the three-dimensionalisation of the LSB, could be the root of the abrupt transition near the leading edge above specific radial locations observed in the literature (Schülein *et al.* 2012; Lang *et al.* 2015). This effect is independent of rotation, but the latter may change the location of start and growth rate of the absolute instability.

3.3. *Outboard blade region: large rotation speed variation*

3.3.1. *Flow characteristics*

This section investigates the role of increasing rotation speed (Ro_c) for the same Ro_r (or angle of attack) of cases 4A and 4B. This is equivalent to moving towards lower radial locations so that the free stream azimuthal velocity remains constant. Case 4C presents $Ro_c = 0.1570$ ($r = 6.08$), a rotation rate three times higher than case 4A. Figure 13 shows the isosurfaces of $\lambda_2 = -100$ coloured by the streamwise velocity for case 4C. The LSB moves downstream ($x = 0.033$–0.113) compared with cases 4A and 4B, presenting a much lower height (see table 2). Furthermore, the higher Ro_c suppresses the turbulence wedges, delaying the transition to $x = 0.073$, which suggests the mitigation of the global mode that three-dimensionalises the LSB and absolute secondary instability of the KH rolls. The latter develops 16 hairpin structures or lambda vortices ($\beta = 402.1$, $\beta\delta^* = 0.7$, or $n_z = 16$)
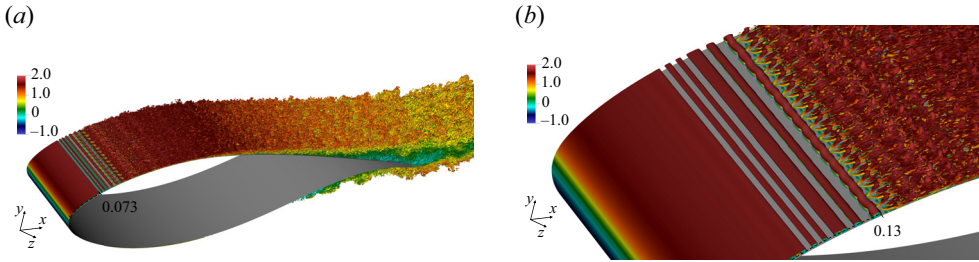
999 A54-16

(*a*)

(*b*)

Figure 13. The λ_2-structures ($\lambda_2 = -100$) coloured by the streamwise velocity for case 4C. Panel (*b*) shows a magnified view of transition.

along the span before breakdown to turbulence, as highlighted in figure 13(*b*). The secondary instability of KH modes in separated shear layers may lead to the appearance of streamwise vortical structures ('ribs') in the braid region between rolls in the fundamental case (Jones, Sandberg & Sandham 2008; Marxen, Lang & Rist 2013) and vortex pairing, doubling the streamwise wavelength, in the subharmonic case (Metcalfe *et al.* 1987; Lin & Pauley 1996; McAuliffe & Yaras 2009; Fava *et al.* 2023*b*). However, 'ribs' and vortex pairing are not observed. This is possible due to a thin separated shear layer, with a strong wall influence, where the primary mode has characteristics of TS waves (Rist & Maucher 2002). Lambda vortices have been observed in other studies on short LSBs (Alam & Sandham 2000; Burgmann & Schröder 2008; Brinkerhoff & Yaras 2011). In the fundamental or K-type resonance (Klebanoff, Tidstrom & Sargent 1962), TS waves interact with a pair of oblique waves of the same frequency, whereas in the subharmonic or H-type resonance (Herbert 1988), the oblique disturbances present half the frequency of the TS waves. A detuned resonance is also possible but rare (Liu, Zaki & Durbin 2008). These mechanisms lead to the formation of lambda vortices, which seem staggered considering two consecutive rows in the streamwise direction, suggesting a subharmonic mechanism. Note that unsteady, three-dimensional disturbances, as introduced in the simulations, favour the subharmonic route (Marxen & Rist 2010). Nevertheless, removing or modifying the noise source did not affect the hairpin vortices. Moreover, $\beta = 402.1$ agrees well with the most amplified subharmonic secondary instability mode in an LSB over an aerofoil studied by Maucher, Rist & Wagner (2000) for close values of $Re_{\delta*}$.

Thus, rotation promotes the flow stabilisation in case 4C. Case 4D assesses the effect of a higher rotation rate and more inboard location ($r = 3.04$), with $Ro_c = 0.3140$, six times the values of cases 4A and 4C, respectively. Figure 14 shows the isocontours of $\lambda_2 = -100$ for case 4D for times $T < T_b$, $T \approx T_b$, $T > T_b$, with T_b being the time when cross-flow transition starts. In the first instant, in figure 14(*a*), an LSB is present in the region $x = 0.348$–0.484 with a reverse flow of -10.7% (see table 2). The KH rolls are formed and break down to turbulence, leading to transition at $x_{tr} = 0.448$. Note that this is much more downstream than in case 4C, which allows a considerably larger LSB in case 4D. The cross-flow velocity at the transition location is $u_{cr_{tr}} = -28.3\%$, with the negative sign indicating tip flow. However, this flow configuration abruptly changes at $T \approx T_b$, as depicted in figure 14(*b*), where oblique structures are present in $x = 0.33$–0.37. This is better seen in region T of figure 14(*d*). One can define the angle $\Psi = \Phi - \eta$, where $\Phi = \arctan(\beta/\alpha_r)$ is the wave angle associated with the wavevector $\boldsymbol{k} = (\alpha_r, \beta)$, and $\eta = \arctan(W_e/U_e)$ is the angle of the inviscid streamline $\boldsymbol{U_e} = (U_e, W_e)$ (Arnal & Casalis 2000). Here, $\Phi \approx -60°$ and $\eta \approx 31°$, which yields $\Psi \approx -91°$. This value of Ψ agrees with those of cross-flow modes (Saric *et al.* 2003). Furthermore, the LST
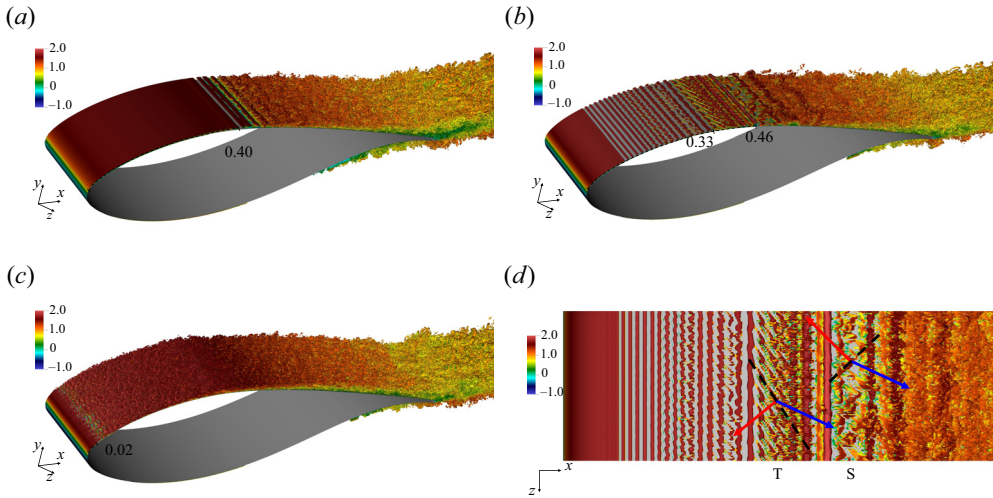
Figure 14. The λ_2-structures ($\lambda_2 = -100$) coloured by the streamwise velocity for case 4D: (*a*) $T < T_b$; (*b*) $T \approx T_b$; (*c*) $T > T_b$; (*d*) $T \approx T_b$. In (*d*), T and S denote the travelling and stationary cross-flow modes. The wavevector ($\boldsymbol{k}$) and inviscid streamline vector ($\boldsymbol{U_e}$) are represented with red and blue arrows, respectively.
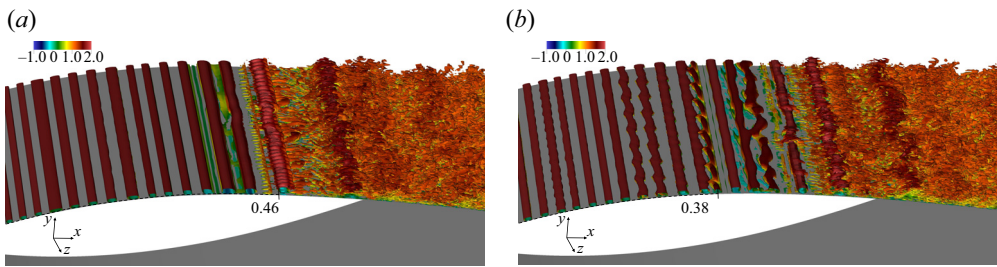

Figure 15. Detailed view of the λ_2-structures ($\lambda_2 = -100$) coloured by the streamwise velocity for $T = T_1 < T_b$ in (*a*) and $T = T_2$ such that $T_1 < T_2 < T_b$ in (*b*) for case 4D.

results of Gross *et al.* (2012) for a rotating blade indicate $\Phi = -60.9°$ for the most unstable travelling cross-flow mode ($f = 15.9$ and $\beta = 180$), which nearly agrees with the wave angle observed in the current simulations. It is also worth noting that $n_z = 7.16$ for $\beta = 180$, almost matching the eight vortices along z in figure 14(*d*). Three oblique vortices appear in $x = 0.46$–0.51 (region S). They are inclined in a different direction than the travelling cross-flow modes and present $\Phi \approx 55°$ and $\eta \approx 36°$, giving $\Psi \approx +91°$. This value matches that obtained by Gross *et al.* (2012) for the most unstable stationary cross-flow disturbance ($f = 0$ and $\beta = 70$). Furthermore, $\beta = 70$ corresponds to $n_z = 2.79$, nearly agreeing with the three vortices in the simulations. Observe that the travelling cross-flow modes form near the leading edge of the LSB, whereas the stationary ones appear close to reattachment. Gross *et al.* (2012) found that the stationary modes were more unstable than the travelling ones. This is unlike swept-wing flows, where the latter typically dominates (Borodulin *et al.* 2019).

Figure 15 shows a detailed view of the KH rolls at two time instants T_1 and $T_2 > T_1$ before cross-flow transition. At T_1, the rolls undergo a fundamental secondary instability where ribs form in the braid region between rolls (Metcalfe *et al.* 1987). The large number of filaments along the span resembles the short wavelength instability described by

999 A54-18

He *et al.* (2017). At the later time T_2, the KH rolls display a spanwise modulation with eight wavelengths, the same as the travelling cross-flow modes, suggesting the latter introduces a secondary instability into the former, leading to premature breakdown of the rolls. The modulation of the base flow is a known feature of cross-flow modes, which saturates when their amplitude reaches 20 % (Saric *et al.* 2003). The saturated state can persist long before high-frequency convective secondary instabilities are excited, rapidly breaking down to turbulence (Wassermann & Kloker 2002), as seen here. The most unstable secondary instability frequency is one order higher than that of the primary mode, with the sinuous mechanism typically being the most unstable, followed by the varicose one (Malik, Li & Chang 1994; Malik *et al.* 1999). After the start of cross-flow transition ($T > T_b$), the transition line moves to the leading edge, as shown in figure 14(*c*). The cross-flow velocity presents an exceedingly high value of -56 % at the transition location (see table 2), and the structures forming there resemble cross-flow vortices. Case 4D is prone to cross-flow instabilities due to the higher rotation, which generates a higher cross-flow since u_z scales with Ro_c (see (2.5)). In particular, $u_{cr} \approx -30$ % where stationary and cross-flow modes first appear, much higher than the 5 %–10 % required for this instability (Arnal & Casalis 2000). These high cross-flow values are enabled particularly in the LSB, where the reverse flow provides a means for rotation to generate a cross-flow profile, which presents an S shape and is highly unstable. The fact that APG is lower in case 4D also allows transition via the cross-flow mechanism since its growth is not bypassed by that of TS and KH modes (Arnal & Casalis 2000; Borodulin *et al.* 2019).

3.3.2. *Spectral and stability analyses*

Local LST analyses are performed for cases 4C and 4D. Since the flow is sufficiently spanwise-uniform, the base flow is assumed to be the spanwise- and time-averaged flow. The most unstable disturbances in case 4C, corresponding to KH modes, present maximum amplification near the leading edge, followed by a stabilisation as the flow transitions. The growth rates are lower than those from cases 4A and 4B, confirming the stabilisation promoted by rotation. Considering case $4D\ T < T_b$, the highest growth rates occur at $x = 0.41$ since the LSB and transition are delayed by rotation. Case $4D\ T > T_b$ presents high amplification near the leading edge, surpassing case 4C. The unstable region is relatively short due to the quick turbulent breakdown. Figure 16(*b*) shows the frequency neutral curve for the most unstable β. The most unstable frequencies (line with circles) are relatively close, considering cases 4C and 4D, and linked to KH modes. The relatively high frequency of the modes near the leading edge explains the considerable amplitude observed in the spectra for frequencies such as $f = 80\text{–}90$. The most unstable mode frequency quickly drops with x, scaling inversely with the boundary-layer thickness (Brinkerhoff & Yaras 2011). This frequency converges to that of travelling cross-flow modes ($f \approx 16$) as x increases in case $4C\ T > T_b$, especially for $x > 0.13$. Note that the cross-flow modes only become the most unstable disturbance near reattachment. Before that, the KH instability displays the maximum growth.

Figure 17(*a*) shows the growth rates as a function of f and β for cases 4D:- $T < T_b$ and $T > T_b$ at specific streamwise locations. There are two unstable regions at $x = 0.43$ for case 4D ($T < T_b$) in figure 17(*a*). The highest growth rates occur for $f = 25$, $\beta = 75$ ($\beta\delta^* = 0.4$), corresponding to a KH mode under the influence of spanwise flow. A second region, centred at $f = 10$, $\beta = 425$ ($\beta\delta^* = 2.3$), is associated with travelling cross-flow modes with lower growth rates than the KH modes. Stationary cross-flow modes present reduced growth rates than the travelling ones. However, stationary modes display growth
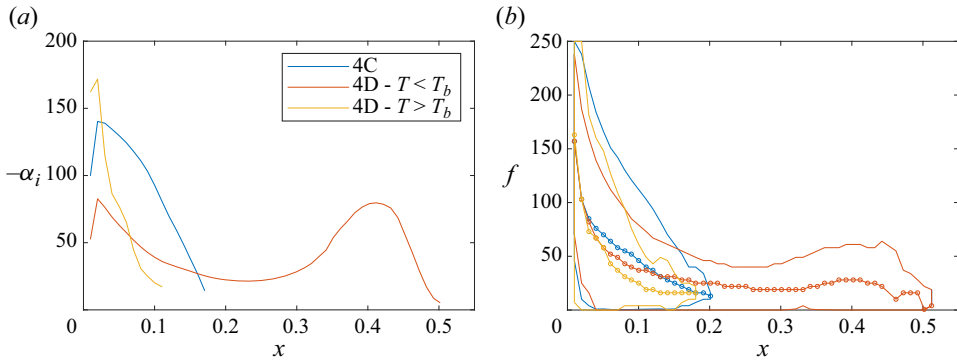
Figure 16. (*a*) Growth rate (maximum over f and β) and (*b*) neutral curve (maximum over β) from local LST for several spanwise slices of the time-averaged flow of cases 4C and 4D. The line with circles in the neutral curve indicates the most-unstable frequency.
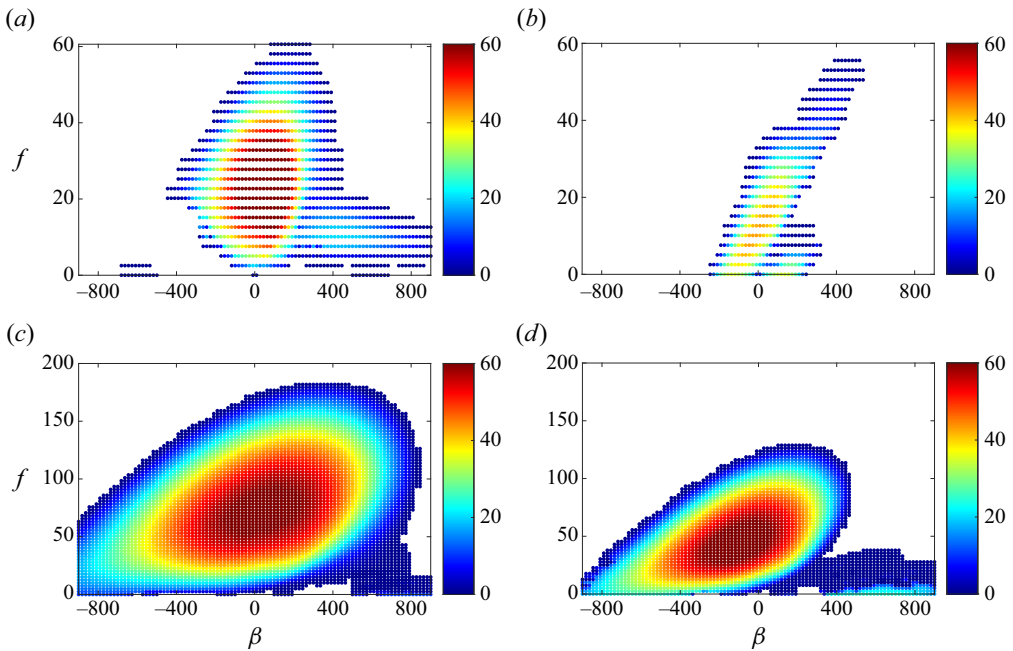

Figure 17. Growth rate from LST at specific streamwise locations as a function of the frequency and spanwise wavenumber for case 4D: (*a*) $T < T_b$ - $x = 0.43$; (*b*) case 4D $T < T_b$ - $x = 0.46$; (*c*) $T > T_b$ - $x = 0.03$; (*d*) $T > T_b$ - $x = 0.06$.

rates comparable to the KH instability at $x = 0.46$ in figure 17(*b*). The dominance of stationary cross-flow modes near flow reattachment agrees with the simulations. Considering case 4D ($T > T_b$) at $x = 0.03$ in figure 17(*c*), the maximum amplification occurs at $f = 73$, $\beta = 50$ ($\beta\delta^* = 0.06$), corresponding to a KH mode. However, travelling cross-flow modes also present non-negligible growth rates. Farther downstream, at $x = 0.06$ in figure 17(*d*), stationary cross-flow modes exhibit higher amplification. These results support the presence of cross-flow modes in case 4D. Note that the structures ultimately appearing depend on the integrated growth rate (N factor).
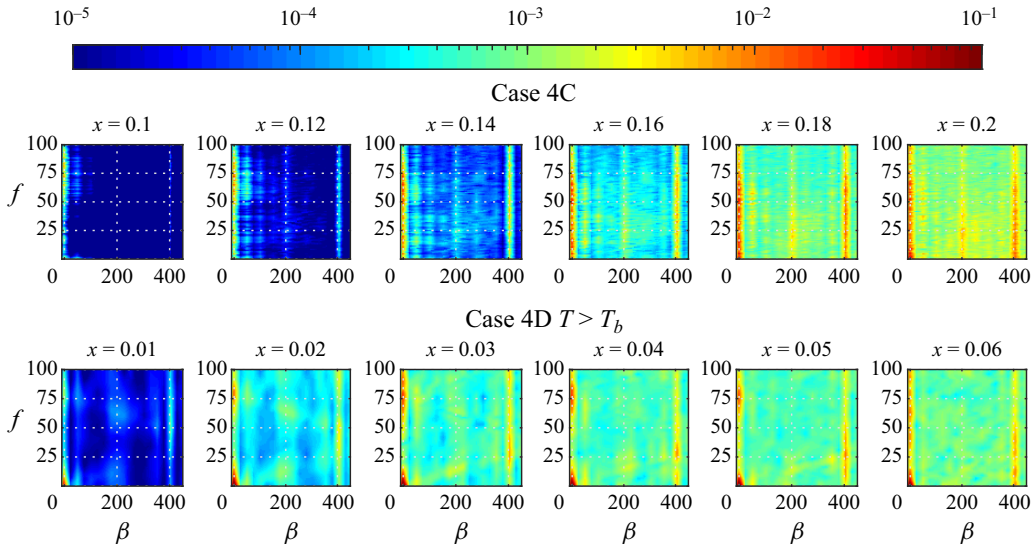
999 A54-20

Figure 18. Spectra of streamwise velocity perturbations ($|u'|$) at $y = \delta^*$ for cases 4C and 4D - $T > T_b$.

Figure 18 shows the $|u'|$ boundary-layer spectra for case 4C. The KH instability occurs over the $\beta = 0$ line for several frequencies. The secondary instability of the KH rolls generates the 16 hairpin vortices with $\beta = \pm 402.1$ ($\beta\delta^* \pm 0.7$), especially for $x \geq 0.12$. Nonlinear interactions lead to the excitation of $\beta = \pm 402.1 n/2$, $n = 1, 2, 3, 4$ disturbances. Considering case 4D ($T > T_b$) in figure 18, there are two regions of primary instability – the $\beta = 0$ disturbances, associated with the KH modes formed in the short LSB near the leading edge and $f \approx 15$, $\beta = \pm 201.05$ ($\beta\delta^* \pm 0.2$) perturbations, related to travelling cross-flow modes, as predicted by LST analysis. Disturbances with $\beta = \pm 402.1$ ($\beta\delta^* \pm 0.4$) also present high amplitude. They may be excited by nonlinear interactions between the cross-flow and KH modes and present lower amplitude than in case 4C due to a faster breakdown to turbulence.

3.4. *Effect of a lower adverse pressure gradient*

3.4.1. *Flow characteristics*

As shown in figure 2, cases 5A and 5B present a much lower APG on the suction side than cases 4A–4D, particularly for $x < 0.5$, due to a reduced *AoA* (higher Ro_r). This condition contributes to enhanced cross-flow effects (Du & Selig 2000; Borodulin *et al.* 2019). Figure 19 presents the $\lambda_2 = -100$ isosurfaces coloured by streamwise velocity for cases 5A and 5B. The lower APG allows a large region of laminar flow. The flow becomes unstable due to an LSB in $x = 0.350$–0.558 in case 5A and $x = 0.328$–0.523 in case 5B (see table 2), thus indicating that rotation delays separation. The KH rolls form at $x = 0.5$ in the former case and $x = 0.45$ in the latter. Transition is only slightly moved downstream by rotation from $x = 0.467$ to $x = 0.479$. Interestingly, the maximum reverse flow decreases from -20.6% in the non-rotating case to -6.7% in the rotating case, which is the opposite behaviour of that for high *AoA* (see cases 4A and 4B and Fava *et al.* (2024)). This change could be enough to shift the instability mechanism from absolute in case 5B to convective in case 5A (Huerre & Monkewitz 1990). A weak spanwise modulation of the KH rolls occurs, generated by an oblique streamwise vorticity pattern, as shown in
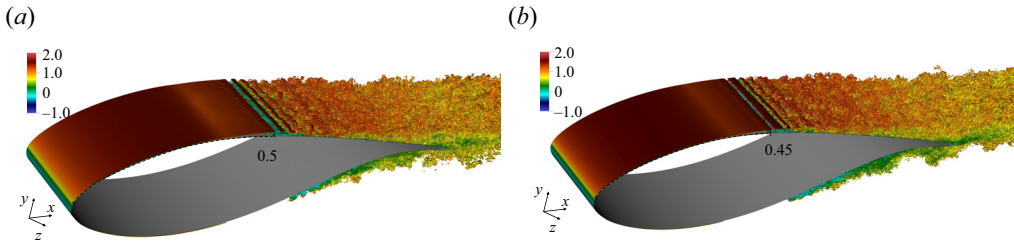
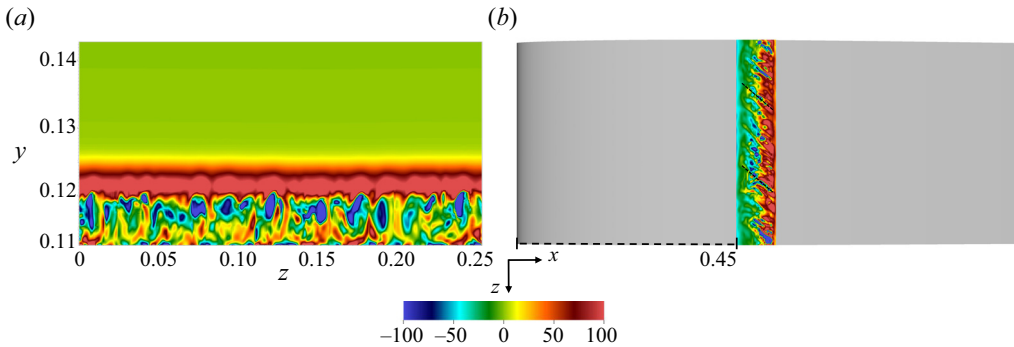Figure 19. The λ_2-structures ($\lambda_2 = -100$) coloured by the streamwise velocity for cases 5A and 5B.

Figure 20. Isocontours of streamwise vorticity for case 5A over a plane at $x = 0.5$ (*a*) and a plane at $y = 0.12$ for $x = 0.45 - 0.52$ (*b*).

figure 20. Figure 20(*b*) shows these contours over a plane on the suction side, providing more explicit evidence of oblique vortices, which resemble the travelling cross-flow modes in case 4D (figure 14*d*). The measured wave angle is $\Phi \approx -50°$, which yields $\Psi \approx -68°$ given that $\eta \approx 18°$.

3.4.2. *Spectral and stability analyses*

Figure 21(*a*) exhibits the LST results for the maximum growth rates for cases 5A and 5B. Case 5B is unstable from the leading edge, whereas unstable modes only appear at $x = 0.14$ in case 5A, indicating a stabilising rotation role. Furthermore, separation is delayed from $x = 0.33$ in case 5B to $x = 0.35$ in case 5A. These effects are related to rotation countering the APG in the attached boundary layer, as observed by Fava *et al.* (2024). The growth rates increase for $x > 0.26$ because the streamwise velocity profiles become inflectional, allowing inviscid instabilities. A sharp peak appears near the transition location ($x_{tr} \approx 0.48$) in the rotating case, where the growth rate nearly doubles. The cross-flow velocity reaches -11.6% there. This feature is absent in the non-rotating case. Figure 21(*b*) presents the frequency neutral curve. High-frequency TS waves occur in case 5B since they appear near the leading edge, where the boundary layer is thin. A broad range of modes become unstable upon separation, including steady disturbances (Dovgal *et al.* 1994). The most unstable modes coincide for cases 5A and 5B until immediately upstream of the transition location. However, in the rotating case, the frequency of the most unstable mode drops considerably in the region $x = 0.48–0.49$. These modes are linked to the spike in amplification.

Further insight into these modes is obtained with the contours of growth rates as a function of f and β. Figures 22(*a*) and 22(*b*) indicate that the KH mode centred at $f = 25$
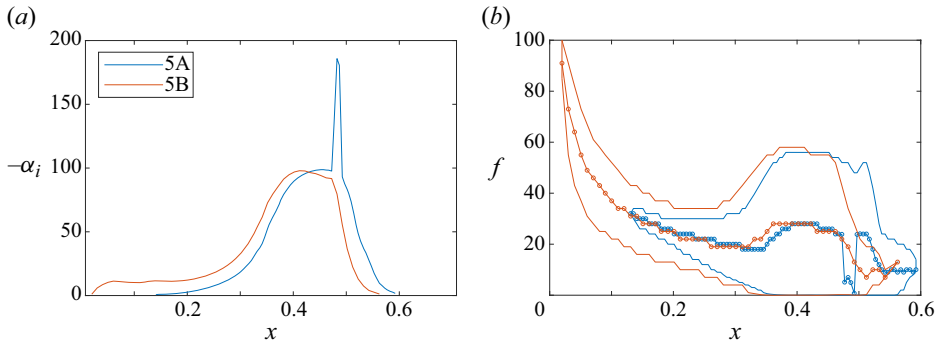
Figure 21. (*a*) Growth rate (maximum over f and β) and (*b*) neutral curve (maximum over β) from local LST the spanwise- and time-averaged flow of cases 5A and 5B. The line with circles in the neutral curve indicates the frequency of the most unstable disturbance.
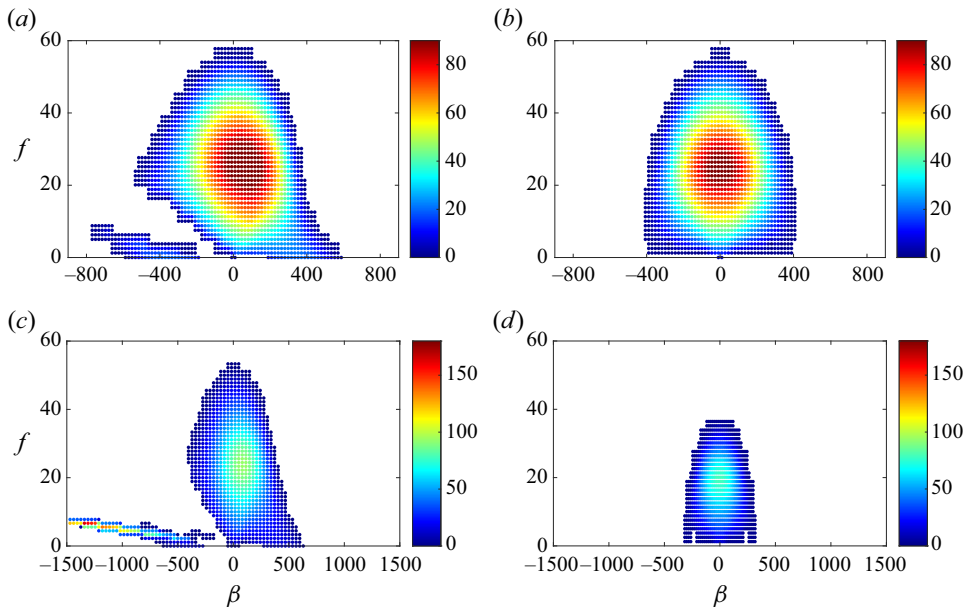

Figure 22. Growth rate from LST at specific streamwise locations as a function of the frequency and spanwise wavenumber for cases 5A (*a,c*) and 5B (*b,d*). Panels (*a,b*) are for $x = 0.45$ and (*c,d*) are for $x = 0.48$.

is the most unstable at $x = 0.45$, although rotation shifts it from $\beta = 0$ to $\beta = 75$ due to the spanwise flow (Toppings & Yarusevych 2023). The rotating case also has low-frequency weak travelling and stationary cross-flow modes on both sides of the $\beta = 0$ line. The KH modes ultimately lead to transition in the non-rotating case. Figure 22(*c*) shows that low-frequency cross-flow modes with $\beta < 0$ develop very high amplification in the rotating case at $x = 0.48$, responsible for the peak noted in the $-\alpha_i$ curves. The mode shape agrees with cross-flow modes (Borodulin *et al.* 2019; Fava *et al.* 2024), which seem to trigger transition in case 5A. However, the transition location is slightly delayed compared with case 5B due to rotation stabilising the attached boundary layer.

Figure 23 presents the $|u'|$ boundary-layer spectra for cases 5A and 5B. They show high-amplitude disturbances centred around $f \approx 26$, $\beta = 0$. This corresponds to
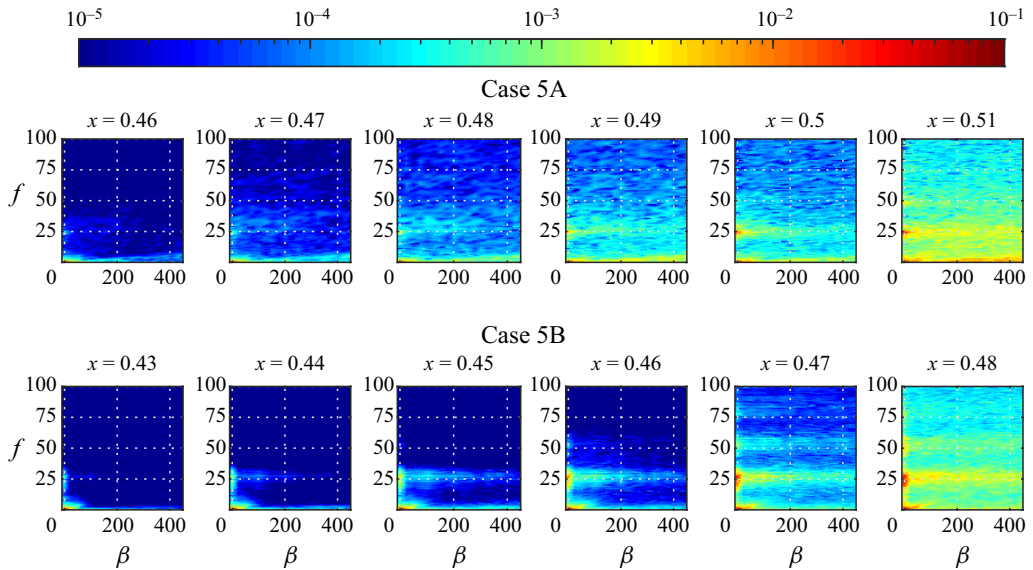
Figure 23. Spectra of streamwise velocity perturbations ($|u'|$) at $y = \delta^*$ for cases 5A and 5B.

$f_s \theta_s / u_s = 0.011$, indicating unstable KH modes (Pauley *et al.* 1990; Brinkerhoff & Yaras 2011). Harmonics with a frequency double the primary instability ($f = 54$) are excited, particularly in case 5B, supporting a fundamental instability and the presence of 'ribs' in the KH rolls. This is much less evident in case 5A, possibly due to rotation counteracting the APG. Case 5A also presents strong fluctuations for $f \lesssim 10$ for $|\beta| \lesssim 1000$ ($|\beta|\delta^* \lesssim$ 7.86) at $x = 0.47$–0.48, corresponding to travelling cross-flow modes, as predicted by LST in figure 22(*c*). The spectra become noisy soon downstream due to transition at $x = 0.47$. These modes do not occur in case 5B. Although transition starts earlier in this case, the breakdown is slower than that triggered by the cross-flow modes in case 5A (Fava *et al.* 2024).

3.4.3. *The role of a lower adverse pressure gradient on cross-flow transition*

Raising Ro_r for fixed Re_c and Ro_c reduces the APG on the suction side, as shown in figure 2, retarding separation and transition. The appearance of strong cross-flow modes at the transition location in case 5A indicates that this instability plays a role in transition. The only difference between cases 4C and 5A is the higher Ro_r (and therefore lower *AoA*) in the latter since Ro_c is nearly the same. Although the cross-flow velocity dropped from $-21.6\,\%$ in case 4C to $-11.6\,\%$ in case 5A, the lower APG in case 5A seems conducive to cross-flow transition as also pointed out by Arnal & Casalis (2000) and Borodulin *et al.* (2019).

3.5. *Comparison of disturbance growth and transition locations*

Figure 24 shows the streamwise evolution of the Reynolds stresses and r.m.s. of velocity fluctuations. The $\overline{u'v'}$ stress is often used to predict transition (Yuan *et al.* 2005; Gaponov 2019). Cases 4A, 4B and 4D ($T > T_b$) present pronounced peaks in $\overline{u'v'}$ near the leading edge, indicating an early transition. The maximum $\overline{u'v'}$ occurs in the latter case and is associated with cross-flow transition. Case 4C and 4D ($T < T_b$) display lower and more
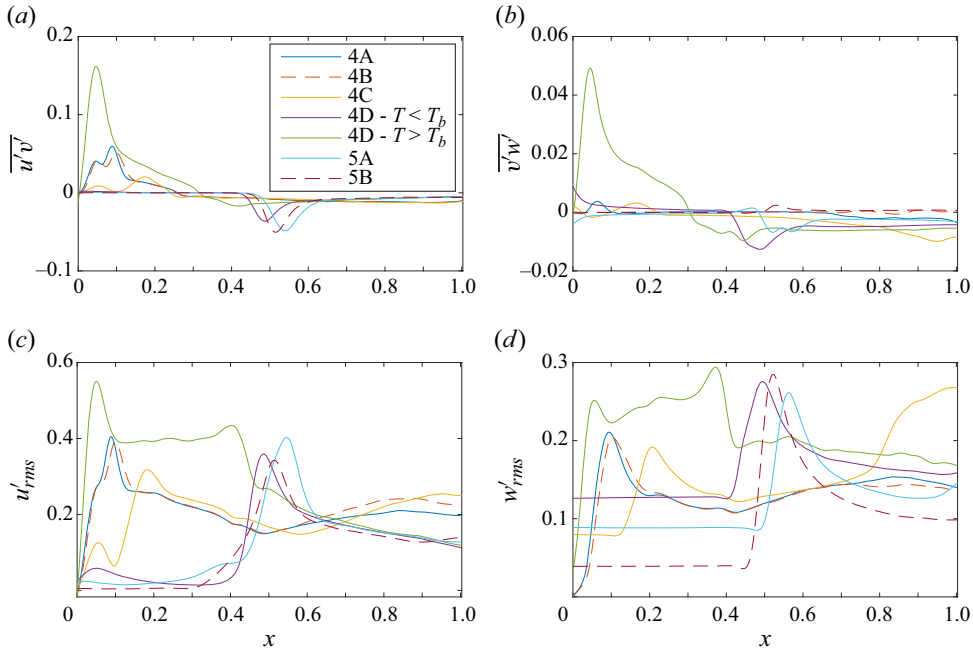
999 A54-24

Figure 24. Maximum over the wall-normal direction of the Reynolds stresses on the longitudinal ($\overline{u'v'}$) and cross-sectional ($\overline{v'w'}$) planes, and r.m.s. of streamwise (u'_{rms}) and spanwise (w'_{rms}) velocity perturbations based on spanwise-averaged statistics.

downstream peaks in $\overline{u'v'}$ due to the stabilising effect of, respectively, low rotation and high rotation in the short term. The negative sign owes to the reversal in $\overline{u'v'}$ after the maximum aerofoil thickness location. Cross-flow transition in case 4D ($T > T_b$) is highlighted by the $\overline{v'w'}$ peak in figure 24(b), considerably higher than other cases and associated with cross-flow intense-fluctuation events. Figures 24(c) and 24(d) present the r.m.s. of u' and w' associated with both KH and cross-flow modes since the latter also produces strong streamwise velocity fluctuations (Saric *et al.* 2003). Cases 4A and 4B show close values of peak u'_{rms} and w'_{rms} since they undergo similar absolute secondary instability mechanisms. However, the increase in Ro_c leads to a continuous rise in w'_{rms} in cases 4C, 4D ($T < T_b$), and 4D ($T > T_b$), as cross-flow instability is enhanced. However, in cases 4C and 4D ($T < T_b$), the maximum u'_{rms} is lower than in cases 4A and 4B and occurs more downstream due to the stabilisation of the KH mechanism by rotation. Regarding cases 5A and 5B, the maxima in u'_{rms} and w'_{rms} are more downstream in the rotating case, underlining the transition delay by rotation.

Figure 25 shows the transition locations as a function of Ro_c for the two values of λ_r (or Ro_r) studied. Considering $\lambda_r = 3.1$, the transition locations are insensitive to rotation in cases 4A and 4B due to the absolute instability of the LSB near the leading edge. Low rotation and, in the short term, high rotation delay separation and transition due to the acceleration of the attached and weakly separated flows. This occurs in cases 4C and 4D ($T < T_b$). Although more downstream, the turbulent breakdown is typically faster when rotation is at play. High rotation shifts transition to the leading edge in the long term due to strong cross-flow instability, as in case 4D ($T > T_b$). Regarding $\lambda_r = 6.3$, the flow remains laminar for a much larger extent than in the previous cases due to a lower *AoA*.
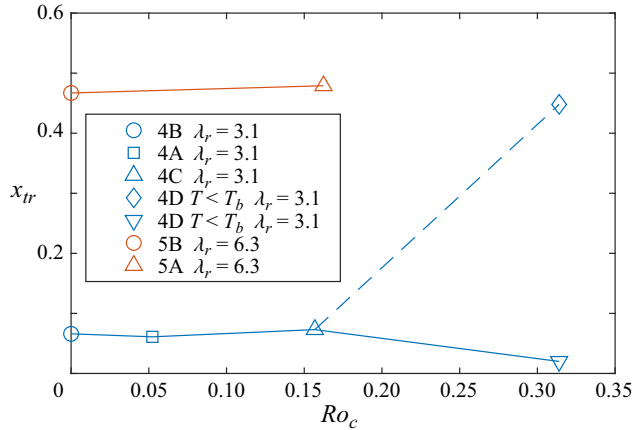
Figure 25. Transition locations as a function of the rotation numbers Ro_c and λ_r.

Compared with $\lambda_r = 3.1$, the main difference is that a strong cross-flow instability is triggered at a lower Ro_c. Although this happens, the acceleration of the attached and weakly separated flows by rotation moves the transition location slightly more downstream in the rotation case.

3.6. *Analysis of the production of disturbance kinetic energy*

The production term ($\mathcal{P}$) in the Reynolds–Orr equation provides further insight into the mechanisms by which the KH and cross-flow modes act to stabilise or destabilise the flow (Schmid & Henningson 2001). Here $\mathcal{P} > 0$ implies that the disturbance kinetic energy may increase over time if it overcomes viscous dissipation. To derive $\mathcal{P}$, the cross-flow perturbation is written in the x'', y'', z'' coordinate system, see figure 26, and is given by $(0, v'', w'')_{CF}$. The KH perturbation is written in the x, y, z coordinate system and reads $(u, v, 0)_{KH}$. The base flow is assumed to be $\bar{U} = \bar{U}(x, y)$, $\bar{V} = \bar{V}(x, y)$, $\bar{W} = \bar{W}(x, y)$. Given all quantities in the x, y, z system, the production term reads

$$\mathcal{P} = \iiint \mathcal{L} \, d\mathcal{V}, \tag{3.1}$$

where the integrand is defined as

$$\begin{aligned}
\mathcal{L} = &-\underbrace{\left[\frac{\partial \bar{U}}{\partial x}\right] \mathcal{R}^2}_{a} - \underbrace{\left[(v_{CF} + v_{KH})\left(\frac{\partial \bar{U}}{\partial y} + \frac{\partial \bar{V}}{\partial x}\right)\right] \mathcal{R}}_{b} - \underbrace{\left[\frac{\partial \bar{W}}{\partial x}\right] \mathcal{R}\mathcal{H}}_{c} \\
&- \underbrace{\left[(v_{CF} + v_{KH})\left(\frac{\partial \bar{W}}{\partial y}\right)\right] \mathcal{H}}_{d} - \underbrace{\left[(v_{KH}^2 - v_{CF}^2)\frac{\partial \bar{U}}{\partial x}\right]}_{e}, \\
\mathcal{R} = &\frac{\sin(2\Delta)}{2} w_{CF} + \left[\frac{\cos(2\Delta) + 1}{2} u_{CF}\right] + u_{KH}, \\
\mathcal{H} = &\frac{\sin(2\Delta)}{2} u_{CF} + \left[\frac{1 - \cos(2\Delta)}{2} w_{CF}\right],
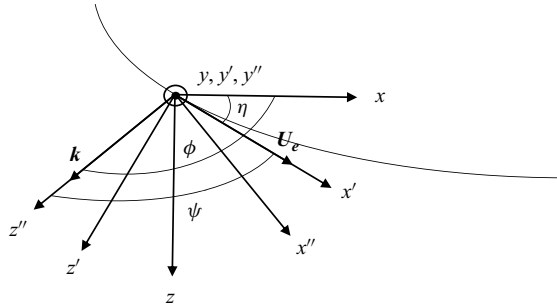\end{aligned} \right\} \tag{3.2}$$

Figure 26. Coordinate system used to derive $\mathcal{P}$. Here x and z are the streamwise and spanwise directions; η is the angle between x and the inviscid streamline $\boldsymbol{U_e} = (u_e, 0, w_e) /\!/ x'$; ϕ is the wave angle, i.e. the angle between x and the wavevector $\boldsymbol{k} = (\alpha, 0, \beta) /\!/ z''$ of the cross-flow mode; $\Psi = \angle(\boldsymbol{k}, \boldsymbol{U_e}) = \phi - \eta$.

with $\Delta = \psi - \eta$; $\mathcal{L}$ is a quadratic polynomial on $\mathcal{R}$ and $\mathcal{H}$, with these functions depending on Δ, assumed to be the only independent variable. Furthermore, it is assumed that $\bar{U}$ varies with x ($a \neq 0$). If there is no streamwise variation of $\bar{W}$ ($c = 0$), the critical points $(\mathcal{R}^*, \mathcal{H}^*)$, such that $\nabla \mathcal{L}(\mathcal{R}^*, \mathcal{H}^*) = \boldsymbol{0}$, are $\mathcal{R}^* = -b/(2a)$ and $\mathcal{H}^* \in \mathbb{R}$. The determinant of the Hessian matrix is simply $\det(\boldsymbol{H}) = \mathcal{L}_{\mathcal{R}\mathcal{R}} = -2a$, which is negative if the flow is accelerating ($a > 0$). In this case, $\mathcal{L}$ has a maximum $\mathcal{L}(\mathcal{R}^*, \mathcal{H}^*) = b^2/(4a) - e$, and the cross-flow perturbations are destabilising if $v_{CF} > v_{KH}$. Conversely, if the flow is decelerating ($a < 0$), $\mathcal{L}(\mathcal{R}^*, \mathcal{H}^*)$ is a minimum and the cross-flow perturbations are stabilising if $v_{CF} > v_{KH}$. From the definition of $\mathcal{R}$ and equating that to $\mathcal{R}^*$, one obtains the critical angle

$$\Delta^* = -\frac{1}{2} \arcsin\left(\frac{b/a + u_{CF} + 2u_{KH}}{\sqrt{u_{CF}^2 + w_{CF}^2}}\right) - \frac{1}{2} \arctan\left(\frac{u_{CF}}{w_{CF}}\right). \tag{3.3}$$

Interestingly, the last term in (3.3) minimises $\mathcal{H}$.

If $\bar{W}$ varies with x ($c \neq 0$), the critical points are $\mathcal{R}^* = -d/c$ and $\mathcal{H}^* = (2ad - bc)/c^2$. However, $\det(\boldsymbol{H}) = -\mathcal{L}_{\mathcal{R}\mathcal{H}}^2 = -c^2 < 0$, indicating that $(\mathcal{R}^*, \mathcal{H}^*)$ is a saddle point of $\mathcal{L}$. This issue may be circumvented by constraining $\mathcal{L}$ over the $\partial\mathcal{L}/\partial\mathcal{R} = 0$ line ($\mathcal{R} = (b + c\mathcal{H})/(2a)$). The critical point of $\mathcal{L} = \mathcal{L}(\mathcal{H})$ is $\mathcal{H}^* = b/c + 4ad/(6c^2)$, from which $\mathcal{R}^* = b/(2a) + 4d/(6c)$ can be computed. Moreover, $\det(\boldsymbol{H}) = \mathcal{L}_{\mathcal{H}\mathcal{H}} = -6c^2/(4a)$. Therefore, if $a > 0$, $\mathcal{L}(\mathcal{H}^*) = -3b^2/a - 3bd/c - ad^2/c^2 - e$ is a maximum. Similar to previously noted for $c = 0$, the cross-flow perturbations are destabilising if $v_{CF} > v_{KH}$. In the case of $a < 0$, $\mathcal{L}(\mathcal{H}^*)$ is a minimum and $v_{CF} > v_{KH}$ leads to a stabilisation. The critical angle is obtained by equating the definition of $\mathcal{H}$ to $\mathcal{H}^*$ and is given by

$$\Delta^* = \frac{1}{2} \arcsin\left(\frac{2b/c + 4ad/(3c^2) - w_{CF}}{\sqrt{u_{CF}^2 + w_{CF}^2}}\right) + \frac{1}{2} \arctan\left(\frac{w_{CF}}{u_{CF}}\right). \tag{3.4}$$

The second term on the right-hand side of (3.4) maximises $\mathcal{R}$. The above discussion indicates that a critical cross-flow mode angle exists, maximising or minimising $\mathcal{P}$ depending on the accelerating or decelerating nature of the flow. Besides, cross-flow perturbations may be stabilising, delaying transition.

4. Conclusions

A numerical investigation of transition on a rotating wind turbine blade is carried out with direct numerical simulations of a blade section at $Re_c = 3 \times 10^5$ in the rotating frame of reference. Six cases with varying rotation numbers Ro_c and Ro_r are considered. The investigations are complemented with spectral and linear stability analyses.

The results indicate that rotation does not substantially affect the transition location in the outboard region of the blade or for low rotation rates. This is because a leading-edge LSB appears and is deformed by a global instability mode. The KH vortices undergo a secondary absolute instability over the deformed LSB, forming turbulence spots at specific spanwise locations. This phenomenon leads to a rapid transition, and rotation effects are not predominant. Moreover, it may explain the fast transition observed in the outboard region of rotating blades in previous works (Schülein *et al.* 2012; Lang *et al.* 2015).

Moderate increases in the rotation rate (Ro_c) stabilise the flow, slightly delaying transition due to the acceleration of the attached boundary layer and possible competition between weak cross-flow and KH modes. Higher rises in Ro_c promote further delay in transition in the short term. However, stationary and travelling cross-flow modes are eventually triggered, modulating the KH rolls and leading to their turbulent breakdown. The transition line rapidly moves to the leading edge, where it lies in the long term. In this case, the cross-flow velocity reaches a value of 56 % at the transition location, with a component directed to the blade tip. A higher value of Ro_r, corresponding to a lower adverse pressure gradient and *AoA*, promotes cross-flow transition at lower rotation rates. However, despite the high growth rates of the travelling cross-flow mode leading to transition in the rotating case, the transition location is farther downstream than in the non-rotating case because rotation stabilises the attached boundary layer.

Thus, there is a threshold of rotation rate above which rotation may trigger cross-flow transition, and this limit seems to decrease with increasing Ro_r. Compared with the non-rotating case, the delay or advancement of the transition line due to rotation depends on the competition between the stabilisation of the attached boundary layer and the inception of cross-flow modes, particularly in the flow separation zone.

Declaration of interests. The authors report no conflict of interest.

Data availability statement. Data are available upon request.

Author ORCIDs.
- T.C.L. Fava https://orcid.org/0009-0007-8056-6109;
- D. Massaro https://orcid.org/0000-0002-6712-8944;
- P. Schlatter https://orcid.org/0000-0001-9627-5903;
- D.S. Henningson https://orcid.org/0000-0001-7864-3071;
- A. Hanifi https://orcid.org/0000-0002-5913-5431.

Appendix A. Operators for one-dimensional local stability analyses

The one-dimensional stability problem is obtained by introducing the ansatz $q' = \hat{q}(y) \exp{(i\alpha x + i\beta z - i\omega t)}$ in the linearised Navier–Stokes equations (equations for the momentum in x, y, z and continuity), accounting for rotation effects, where $q'(x, y, z, t) = [u'\ v'\ w'\ p']^T$ is the vector of perturbations of streamwise (u'), normal (v') and spanwise (w') velocities and pressure (p'). Here $\alpha = \alpha_r + i\alpha_i$, where α_r is the streamwise wavenumber, and α_i is the spatial growth rate. Here $\beta \in \mathbb{R}$ is the spanwise wavenumber. $\omega = 2\pi f \in \mathbb{R}$ is the angular frequency, a parameter in the spatial framework employed here. The resulting eigenvalue problem, solved for α and $\hat{q}$, is given by

$$\mathcal{A}\hat{q} = \alpha \mathcal{B}\hat{q}, \tag{A1}$$

$$\mathcal{A} = \begin{pmatrix} 0 & \mathcal{D}_y & i\beta & 0 \\ \varXi & -\bar{U}_y & -2\Omega_n\bar{W} & 0 \\ 0 & \varXi & 2\Omega_s & -\mathcal{D}_y \\ 2\Omega_n & -\bar{W}_y - 2\Omega_s & -i\beta & 0 \end{pmatrix}, \quad \mathcal{B} = \begin{pmatrix} -i & 0 & 0 & 0 \\ i\bar{U} & 0 & 0 & i \\ 0 & i\bar{U} & 0 & 0 \\ 0 & 0 & i\bar{U} & 0 \end{pmatrix}, \tag{A2a,b}$$

where $\mathcal{D}_y$ is the derivative in the y direction, obtained with a spectral Chebyshev approximation, and $\varXi = 1/Re_c(\mathcal{D}_y^2 - \beta^2) - i(\beta\bar{W} - \omega)$. The vector of base-flow variables is given by $\bar{q} = [\bar{U}\ \bar{V}\ \bar{W}\ \bar{P}]^T$, where $\bar{P}$ is the pressure, and $\bar{U}$, $\bar{V}$ and $\bar{W}$ are the streamwise, normal and spanwise velocities. The base flow is assumed to be the spanwise- and time-averaged flow or a slice at given z of the time-averaged flow, interpolated to a grid with 150 Chebyshev points in the wall-normal direction (y). The subscript y indicates derivative in the y direction; $i = \sqrt{-1}$ is the imaginary unity; Re_c is the Reynolds number; Ω_s and Ω_n are the rotation speeds in the streamwise and normal direction, given by

$$\left.\begin{aligned} \Omega_s &= \Omega \sin\phi \cos\theta + \Omega \cos\phi \sin\theta, \\ \Omega_n &= \Omega \cos\phi \cos\theta - \Omega \sin\phi \sin\theta, \end{aligned}\right\} \tag{A3}$$

where Ω is the rotation rate, ϕ is the twist angle, and θ is the local aerofoil angle. The boundary conditions are u', v', $w' = 0$ at $y = 0$ (wall), $y \to \infty$ (free stream).

Appendix B. Operators for stability analysis over cross-planes

The two-dimensional stability problem is obtained by introducing the ansatz $q' = \hat{q}(y, z) \exp{(i\alpha x - i\omega t)}$ in the linearised Navier–Stokes equations (equations for the momentum in x, y, z and continuity), accounting for rotation effects, where $q'(x, y, z, t) = [u'\ v'\ w'\ p']^T$ is the vector of perturbations of streamwise (u'), normal (v') and spanwise (w') velocities and pressure (p'). Here $\alpha = \alpha_r + i\alpha_i$, where α_r is the streamwise wavenumber, and α_i is the spatial growth rate; $\omega = 2\pi f \in \mathbb{R}$ is the angular frequency, a parameter in the spatial framework employed here. The resulting generalised eigenvalue problem, solved for α, $\hat{q}$, and $\alpha\hat{q}$, is given by

$$\begin{pmatrix} \mathcal{A} & 0 \\ 0 & I \end{pmatrix} \begin{pmatrix} \hat{q} \\ \alpha\hat{q} \end{pmatrix} = \alpha \begin{pmatrix} \mathcal{B} & \mathcal{C} \\ I & 0 \end{pmatrix} \begin{pmatrix} \hat{q} \\ \alpha\hat{q} \end{pmatrix}, \tag{B1}$$

$$\mathcal{A} = \begin{pmatrix} \mathcal{A}_{11} & \bar{U}_y & \bar{U}_z + 2\Omega_n & 0 \\ 0 & \mathcal{A}_{22} & \bar{V}_z - 2\Omega_s & \mathcal{D}_y \\ -2\Omega_n & \bar{W}_y + 2\Omega_s & \mathcal{A}_{33} & \mathcal{D}_z \\ 0 & \mathcal{D}_y & \mathcal{D}_z & 0 \end{pmatrix}, \tag{B2}$$

$$\mathcal{B} = -\begin{pmatrix} i\bar{U} & 0 & 0 & i \\ 0 & i\bar{U} & 0 & 0 \\ 0 & 0 & i\bar{U} & 0 \\ i & 0 & 0 & 0 \end{pmatrix}, \quad \mathcal{C} = -\frac{1}{Re_c}\begin{pmatrix} 1 & 0 & 0 & 0 \\ 0 & 1 & 0 & 0 \\ 0 & 0 & 1 & 0 \\ 0 & 0 & 0 & 0 \end{pmatrix}, \quad \text{(B3}a,b\text{)}$$

$$\mathcal{A}_{11} = \bar{V}\mathcal{D}_y + \bar{W}\mathcal{D}_z - \frac{1}{Re_c}(\mathcal{D}_{yy} + \mathcal{D}_{zz}) - i\omega, \tag{B4}$$

$$\mathcal{A}_{22} = \bar{V}\mathcal{D}_y + \bar{W}\mathcal{D}_z - \frac{1}{Re_c}(\mathcal{D}_{yy} + \mathcal{D}_{zz}) + \bar{V}_y - i\omega, \tag{B5}$$

$$\mathcal{A}_{33} = \bar{V}\mathcal{D}_y + \bar{W}\mathcal{D}_z - \frac{1}{Re_c}(\mathcal{D}_{yy} + \mathcal{D}_{zz}) + \bar{W}_z - i\omega, \tag{B6}$$

where $\mathcal{D}_y$ and $\mathcal{D}_z$ are the derivatives in the y and z directions, obtained with a fourth-order finite-difference approximation. Here $\boldsymbol{I}$ and $\boldsymbol{0}$ are the identity and null matrices. The vector of base-flow variables is given by $\bar{\boldsymbol{q}} = [\bar{U}\ \bar{V}\ \bar{W}\ \bar{P}]^{\mathrm{T}}$, where $\bar{P}$ is the pressure, and $\bar{U}$, $\bar{V}$ and $\bar{W}$ are the streamwise, normal and spanwise velocities. The base flow is assumed to be the time-averaged flow, interpolated to a grid with 700 evenly spaced points in the spanwise direction (z) and 202 geometrically spaced points in the wall-normal direction (y). Subscripts $_y$ and $_z$ indicate derivatives in the y and z directions, respectively. Here $i = \sqrt{-1}$ is the imaginary unity; Re_c is the Reynolds number; Ω_s and Ω_n are defined in equation (A3). The boundary conditions are u', v', $w' = 0$ at $y = 0$ (wall), $y \rightarrow \infty$ (free stream). Periodic boundary conditions are imposed in the spanwise direction, such that $\boldsymbol{q}'(x, y, z, t) = \boldsymbol{q}'(x, y, z + L_z, t)$, where L_z is the spanwise width.

REFERENCES

ALAM, M. & SANDHAM, N.D. 2000 Direct numerical simulation of 'short' laminar separation bubbles with turbulent reattachment. *J. Fluid Mech.* **410**, 1–28.

ALFREDSSON, P.H. & PERSSON, H. 1989 Instabilities in channel flow with system rotation. *J. Fluid Mech.* **202**, 543–557.

ANDERSSON, P., BRANDT, L., BOTTARO, A. & HENNINGSON, D.S. 2001 On the breakdown of boundary layer streaks. *J. Fluid Mech.* **428**, 29–60.

ARNAL, D. & CASALIS, G. 2000 Laminar-turbulent transition prediction in three-dimensional flows. *Prog. Aerosp. Sci.* **36** (2), 173–191.

AVANCI, M.P., RODRÍGUEZ, D. & ALVES, L.S.D.B. 2019 A geometrical criterion for absolute instability in separated boundary layers. *Phys. Fluids* **31** (1), 014103.

BAK, C., BITSCHE, R.D., YDE, A. & KIM, T. 2012 Light rotor: the 10-MW reference wind turbine. In *Proceedings of EWEA 2012 - European Wind Energy Conference and Exhibition*, pp. 1–10.

BALACHANDAR, S., STREETT, C.L. & MALIK, M.R. 1992 Secondary instability in rotating-disk flow. *J. Fluid Mech.* **242**, 323–347.

BJÖRCK, A. 1990 Coordinates and calculations for the FFA-W1-xxx, FFA-W2-xxx and FFA-W3-xxx series of airfoils for horizontal axis wind turbines. *Tech. Rep.* FFA TN 1990-15.

BORODULIN, V.I., IVANOV, A.V., KACHANOV, Y.S., MISCHENKO, D.A., ÖRLÜ, R., HANIFI, A. & HEIN, S. 2019 Experimental and theoretical study of swept-wing boundary-layer instabilities. Unsteady crossflow instability. *Phys. Fluids* **31** (6), 064101.

BOSSCHERS, J. 1995 Influence of blade rotation on the sectional aerodynamics of rotational blades. *Tech. Rep.* National Aerospace Laboratory NLR.

BOUTILIER, M.S.H. & YARUSEVYCH, S. 2012 Separated shear layer transition over an airfoil at a low Reynolds number. *Phys. Fluids* **24** (8), 084105.

BRANDT, L., SCHLATTER, P. & HENNINGSON, D.S. 2004 Transition in boundary layers subject to free-stream turbulence. *J. Fluid Mech.* **517**, 167–198.

BRINKERHOFF, J.R. & YARAS, M.I. 2011 Interaction of viscous and inviscid instability modes in separation-bubble transition. *Phys. Fluids* **23** (12), 124102.

BURGMANN, S. & SCHRÖDER, W. 2008 Investigation of the vortex induced unsteadiness of a separation bubble via time-resolved and scanning PIV measurements. *Exp. Fluids* **45** (4), 675–691.

CHAVIAROPOULOS, P.K. & HANSEN, M.O.L. 2000 Investigating three-dimensional and rotational effects on wind turbine blades by means of a quasi-3D Navier–Stokes solver. *J. Fluids. Engng* **122** (2), 330–336.

CORTEN, G.P. 2001 Flow separation on wind turbine blades. PhD thesis, Utretcht University.

DECHAMPS, X. & HEIN, S. 2018 Extension of the PSE code NOLOT for transition analysis in rotating reference frames. In *New Results in Numerical and Experimental Fluid Mechanics XI: Contributions to the 20th STAB/DGLR Symposium* (ed. A. Dillmann, G. Heller, E. Krämer, C. Wagner, S. Bansmer, R. Radespiel & R. Semaan), pp. 179–188. Springer.

DEVILLE, M.O., FISCHER, P.F. & MUND, E.H. 2002 *High-Order Methods for Incompressible Fluid Flow*. Cambridge University Press.

DIWAN, S.S. & RAMESH, O.N. 2009 On the origin of the inflectional instability of a laminar separation bubble. *J. Fluid Mech.* **629**, 263–298.

DOLLINGER, C., SORG, M., BALARESQUE, N. & FISCHER, A. 2018 Measurement uncertainty of IR thermographic flow visualization measurements for transition detection on wind turbines in operation. *Expl Therm. Fluid Sci.* **97**, 279–289.

DOVGAL, A.V., KOZLOV, V.V. & MICHALKE, A. 1994 Laminar boundary layer separation: instability and associated phenomena. *Prog. Aerosp. Sci.* **30** (1), 61–94.

DU, Z. & SELIG, M.S 2000 The effect of rotation on the boundary layer of a wind turbine blade. *Renew. Energy* **20** (2), 167–181.

DUMITRESCU, H. & CARDOS, V. 2004 Rotational effects on the boundary-layer flow in wind turbines. *AIAA J.* **42** (2), 408–411.

DUMITRESCU, H. & CARDOS, V. 2012 Inboard stall delay due to rotation. *J. Aircraft* **49** (1), 101–107.

FASEL, H.F. & POSTL, D. 2004 Interaction of separation and transition in boundary layers: direct numerical simulations. In *Sixth IUTAM Symposium on Laminar-Turbulent Transition* (ed. R. Govindarajan), pp. 71–88. Springer.

FAVA, T.C.L., HENNINGSON, D.S. & HANIFI, A. 2024 Boundary layer stability on a rotating wind turbine blade section. *Phys. Fluids* **36** (9), 094128.

FAVA, T.C.L., LOBO, B.A., NOGUEIRA, P.A.S, SCHAFFARCZYK, A.P., BREUER, M, HENNINGSON, D.S. & HANIFI, A 2023*a* Influence of free-stream turbulence on the boundary layer stability of a wind turbine airfoil and near wake. *J. Phys.: Conf. Ser.* **2505** (1), 012002.

FAVA, T.C.L., LOBO, B.A., NOGUEIRA, P.A.S., SCHAFFARCZYK, A.P., BREUER, M., HENNINGSON, D.S. & HANIFI, A. 2023*b* Numerical study of the hydrodynamic stability of a wind-turbine airfoil with a laminar separation bubble under free-stream turbulence. *Phys. Fluids* **35** (8), 084104.

FAVA, T.C.L., LOKATT, M., SØRENSEN, N., ZAHLE, F., HANIFI, A. & HENNINGSON, D. 2021 A simplified model for transition prediction applicable to wind-turbine rotors. *Wind Energy Sci.* **6** (3), 715–736.

FISCHER, P., LOTTES, J. & KERKEMEIER, S. 2008 Nek5000: open source spectral element CFD solver. http://nek5000.mcs.anl.gov.

GAPONOV, S.A. 2019 Reynolds stress as an indicator of the laminar-turbulent transition of a boundary layer and a linear disturbance development in it. In *AIP Conference Proceedings 2125* (ed. V. Fomin), 02006. AIP.

GARRETT, S.J., HUSSAIN, Z. & STEPHEN, S.O. 2010 Boundary-layer transition on broad cones rotating in an imposed axial flow. *AIAA J.* **48** (6), 1184–1194.

GREGORY, N., STUART, J.T. & WALKER, W.S. 1955 On the stability of three-dimensional boundary layers with application to the flow due to a rotating disk. *Phil. Trans. R. Soc. Lond.* A **248** (943), 155–199.

GROSS, A., FASEL, H.F., FRIEDERICH, T. & KLOKER, M.J. 2012 Numerical investigation of rotational augmentation for S822 wind turbine airfoil. *Wind Energy* **15** (8), 983–1007.

HAMMOND, D.A. & REDEKOPP, L.G. 1998 Local and global instability properties of separation bubbles. *Eur. J. Mech.* B*/Fluids* **17** (2), 145–164.

HART, J.E. 1971 Instability and secondary motion in a rotating channel flow. *J. Fluid Mech.* **45** (2), 341–351.

HE, W., GIORIA, R.S., PÉREZ, J.M. & THEOFILIS, V. 2017 Linear instability of low Reynolds number massively separated flow around three NACA airfoils. *J. Fluid Mech.* **811**, 701–741.

HERBERT, T. 1988 Secondary instability of boundary layers. *Annu. Rev. Fluid Mech.* **20** (1), 487–526.

HERNANDEZ, G.G.M. 2012 Laminar-turbulent transition on wind turbines. PhD thesis, DTU.

HIMMELSKAMP, H. 1947 Profile investigations on a rotating airscrew. PhD thesis, Völkenrode MAP.

HOSSEINVERDI, S. & FASEL, H.F. 2016 Direct numerical simulations of laminar-to-turbulent transition in laminar separation bubbles in three-dimensional boundary-layer. In *46th AIAA Fluid Dynamics Conference*. AIAA Paper 2016-3793. AIAA

HUERRE, P. & MONKEWITZ, P.A. 1990 Local and global instabilities in spatially developing flows. *Annu. Rev. Fluid Mech.* **22** (1), 473–537.

HUNT, J.C.R. & CARRUTHERS, D.J. 1990 Rapid distortion theory and the 'problems' of turbulence. *J. Fluid Mech.* **212** (1), 497–432.

JAROSLAWSKI, T., FORTE, M., MOSCHETTA, J.-M., DELATTRE, G. & GOWREE, E.R. 2022 Characterisation of boundary layer transition over a low Reynolds number rotor. *Expl Therm. Fluid Sci.* **130**, 110485.

JAROSLAWSKI, T., FORTE, M., VERMEERSCH, O., MOSCHETTA, J.-M. & GOWREE, E.R. 2023 Disturbance growth in a laminar separation bubble subjected to free-stream turbulence. *J. Fluid Mech.* **956**, A33.

JING, Z. & DUCOIN, A. 2020 Direct numerical simulation and stability analysis of the transitional boundary layer on a marine propeller blade. *Phys. Fluids* **32** (12), 124102.

JING, Z, DUCOIN, A & BRAUD, C 2020 Direct numerical simulation of transitional boundary layers on a horizontal axis wind turbine blade. *J. Phys.: Conf. Ser.* **1618** (5), 052042.

JONES, L.E., SANDBERG, R.D. & SANDHAM, N.D. 2008 Direct numerical simulations of forced and unforced separation bubbles on an airfoil at incidence. *J. Fluid Mech.* **602**, 175–207.

JUNG, Y.S., VIJAYAKUMAR, G., ANANTHAN, S. & Baeder, J. 2022 Local correlation-based transition models for high-Reynolds-number wind-turbine airfoils. *Wind Energy Sci.* **7**, 603–622.

VON KÁRMÁN, T. 1921 Über laminare und turbulente Reibung. *Z. Angew. Math. Mech.* **1** (4), 233–252.

KARTHIKEYAN, N., KALIDASA MURUGAVEL, K., ARUN KUMAR, S. & RAJAKUMAR, S. 2015 Review of aerodynamic developments on small horizontal axis wind turbine blade. *Renew. Sustain. Energy Rev.* **42**, 801–822.

KAWAHARA, G., JIMÉNEZ, J., UHLMANN, M. & PINELLI, A. 2003 Linear instability of a corrugated vortex sheet – a model for streak instability. *J. Fluid Mech.* **483**, 315–342.

KIRK, T.M. & YARUSEVYCH, S. 2017 Vortex shedding within laminar separation bubbles forming over an airfoil. *Exp. Fluids* **58** (5), 43.

KLEBANOFF, P.S., TIDSTROM, K.D. & SARGENT, L.M. 1962 The three-dimensional nature of boundary-layer instability. *J. Fluid Mech.* **12** (1), 1–34.

KOYAMA, H., MASUDA, S., ARIGA, I. & WATANABE, I. 1979 Stabilizing and destabilizing effects of Coriolis force on two-dimensional laminar and turbulent boundary layers. *J. Engng Power* **101** (1), 23–29.

KUPFER, K., BERS, A. & RAM, A.K. 1987 The cusp map in the complex-frequency plane for absolute instabilities. *Phys. Fluids* **30** (10), 3075–3082.

LANG, W., GARDNER, A.D., MARIAPPAN, S., KLEIN, C. & RAFFEL, M. 2015 Boundary-layer transition on a rotor blade measured by temperature-sensitive paint, thermal imaging and image derotation. *Exp. Fluids* **56** (6), 118.

LEZIUS, D.K. & JOHNSTON, J.P. 1976 Roll-cell instabilities in rotating laminar and trubulent channel flows. *J. Fluid Mech.* **77** (1), 153–174.

LIN, J.C.M. & PAULEY, L.L. 1996 Low-Reynolds-number separation on an airfoil. *AIAA J.* **34** (8), 1570–1577.

LINGWOOD, R.J. 1995 Absolute instability of the boundary layer on a rotating disk. *J. Fluid Mech.* **299**, 17–33.

LINGWOOD, R.J. 1996 An experimental study of absolute instability of the rotating-disk boundary-layer flow. *J. Fluid Mech.* **314**, 373–405.

LIU, Y., ZAKI, T.A. & DURBIN, P.A. 2008 Floquet analysis of secondary instability of boundary layers distorted by Klebanoff streaks and Tollmien–Schlichting waves. *Phys. Fluids* **20** (12), 124102.

MALIK, M.R. 1986 The neutral curve for stationary disturbances in rotating-disk flow. *J. Fluid Mech.* **164**, 275–287.

MALIK, M.R., LI, F. & CHANG, C. -L. 1994 Crossflow disturbances in three-dimensional boundary layers: nonlinear development, wave interaction and secondary instability. *J. Fluid Mech.* **268**, 1–36.

MALIK, M.R., LI, F., CHOUDHARI, M.M. & CHANG, C.-L. 1999 Secondary instability of crossflow vortices and swept-wing boundary-layer transition. *J. Fluid Mech.* **399**, 85–115.

MALIK, M.R., WILKINSON, S.P. & ORSZAG, S.A. 1981 Instability and transition in rotating disk flow. *AIAA J.* **19** (9), 1131–1138.

MARANT, M. & COSSU, C. 2018 Influence of optimally amplified streamwise streaks on the Kelvin–Helmholtz instability. *J. Fluid Mech.* **838**, 478–500.

MARXEN, O., LANG, M. & RIST, U. 2013 Vortex formation and vortex breakup in a laminar separation bubble. *J. Fluid Mech.* **728**, 58–90.

MARXEN, O., LANG, M., RIST, U. & WAGNER, S. 2003 A combined experimental/numerical study of unsteady phenomena in a laminar separation bubble. *Flow Turbul. Combust.* **71**, 133–146.

MARXEN, O. & RIST, U. 2010 Mean flow deformation in a laminar separation bubble: separation and stability characteristics. *J. Fluid Mech.* **660**, 37–54.

MASSARO, D. 2024 Space-adaptive simulation of transition and turbulence in shear flows. PhD thesis, KTH Royal Institute of Technology.

MASSARO, D., LUPI, V., PEPLINSKI, A. & SCHLATTER, P. 2023*a* Global stability of 180°-bend pipe flow with mesh adaptivity. *Phys. Rev. Fluids* **8**, 113903.

MASSARO, D., PEPLINSKI, A. & SCHLATTER, P. 2023*b* Coherent structures in the turbulent stepped cylinder flow at $Re_D = 5000$. *Intl J. Heat Fluid Flow* **102**, 109144.

MASSARO, D., PEPLINSKI, A. & SCHLATTER, P. 2023*c* The flow around a stepped cylinder with turbulent wake and stable shear layer. *J. Fluid Mech.* **977**, A3.

MASSARO, D., PEPLINSKI, A. & SCHLATTER, P. 2023*d* Interface discontinuities in spectral-element simulations with adaptive mesh refinement. In *Spectral and High Order Methods for Partial Differential Equations ICOSAHOM 2020+1* (ed. J.M. Melenk, I. Perugia, J. Schöberl & C. Schwab), pp. 375–386. Springer International.

MASSARO, D., PEPLINSKI, A., STANLY, R., MIRZAREZA, S., LUPI, V., MUKHA, T. & SCHLATTER, P. 2024 A comprehensive framework to enhance numerical simulations in the spectral-element code Nek5000. *Comput. Phys. Commun.* **302**, 109249.

MASSARO, D. & SCHLATTER, P. 2024 Global stability of the flow past a stepped cylinder. *J. Fluid Mech.* **988**, A1.

MASUDA, S. & MATSUBARA, M. 1990 Visual study of boundary layer transition on rotating flat plate. In *Laminar-Turbulent Transition* (ed. D. Arnal & R. Michel), pp. 465–474. Springer.

MAUCHER, U., RIST, U. & WAGNER, S. 2000 Secondary disturbance amplification and transition in laminar separation bubbles. In *Laminar-Turbulent Transition* (ed. H.F. Fasel & W.S. Saric), pp. 657–662. Springer.

MAVRIPLIS, C. 1989 Nonconforming discretizations and a posteriori error estimators for adaptive spectral element techniques. PhD thesis, MIT.

MCAULIFFE, B.R. & YARAS, M.I. 2009 Passive manipulation of separation-bubble transition using surface modifications. *J. Fluids Engng* **131** (2), 021201.

MCCROSKEY, W.J. 1971 Measurements of boundary layer transition, separation and streamline direction on rotating blades. *NASA Tech. Rep.* TN D-6321.

MCCROSKEY, W.J. & YAGGY, P.F. 1968 Laminar boundary layers on helicopter rotors in forward flight. *AIAA J.* **6** (10), 1919–1926.

METCALFE, R.W., ORSZAG, S.A., BRACHET, M.E., MENON, S. & RILEY, J.J. 1987 Secondary instability of a temporally growing mixing layer. *J. Fluid Mech.* **184**, 207–243.

MICHELIS, T., YARUSEVYCH, S. & KOTSONIS, M. 2018 On the origin of spanwise vortex deformations in laminar separation bubbles. *J. Fluid Mech.* **841**, 81–108.

NEGI, P.S., SCHLATTER, P. & HENNINGSON, D.S. 2017 A re-examination of filter-based stabilization for spectral-element methods. *Tech. Rep.* Royal Institute of Technology.

OFFERMANS, N. 2019 Aspects of adaptive mesh refinement in the spectral element method. PhD thesis, Royal Institute of Technology.

OFFERMANS, N., MASSARO, D., PEPLINSKI, A. & SCHLATTER, P. 2023 Error-driven adaptive mesh refinement for unsteady turbulent flows in spectral-element simulations. *Comput. Fluids* **251**, 105736.

PASCAL, L., BARRIER, R., BILLONET, G. & MARTY, J. 2020 Linear stability analysis in rotating frames for fan blade transition prediction. *AIAA J.* **58** (8), 3264–3271.

PATERA, A.T. 1984 A spectral element method for fluid dynamics: laminar flow in a channel expansion. *J. Comput. Phys.* **54** (3), 468–488.

PAULEY, L.L., MOIN, P. & REYNOLDS, W.C. 1990 The structure of two-dimensional separation. *J. Fluid Mech.* **220**, 397–411.

PEPLINSKI, A., OFFERMANS, N., FISCHER, P.F. & SCHLATTER, P. 2020 Non-conforming elements in Nek5000: pressure preconditioning and parallel performance. In *Spectral and High Order Methods for Partial Differential Equations ICOSAHOM 2018. Lecture Notes in Computational Science and Engineering* (ed. S.J. Sherwin, D. Moxey, J. Peiró, P.E. Vincent & C. Schwab), pp. 599–609. Springer International.

POTTER, M.C. & CHAWLA, M.D. 1971 Stability of boundary layer flow subject to rotation. *Phys. Fluids* **14** (11), 2278.

REICHSTEIN, T., SCHAFFARCZYK, A.P., DOLLINGER, C., BALARESQUE, N., SCHÜLEIN, E., JAUCH, C. & FISCHER, A. 2019 Investigation of laminar–turbulent transition on a rotating wind-turbine blade of multimegawatt class with thermography and microphone array. *Energies* **12** (11), 2102.

RIST, U. & MAUCHER, U. 2002 Investigations of time-growing instabilities in laminar separation bubbles. *Eur. J. Mech.* B*/Fluids* **21** (5), 495–509.

RODRÍGUEZ, D. & GENNARO, E.M. 2019 Enhancement of disturbance wave amplification due to the intrinsic three-dimensionalisation of laminar separation bubbles. *Aeronaut. J.* **123** (1268), 1492–1507.

RODRÍGUEZ, D., GENNARO, E.M. & JUNIPER, M.P. 2013 The two classes of primary modal instability in laminar separation bubbles. *J. Fluid Mech.* **734**, R4.

RODRÍGUEZ, D., GENNARO, E.M. & SOUZA, L.F. 2021 Self-excited primary and secondary instability of laminar separation bubbles. *J. Fluid Mech.* **906**, A13.

RODRÍGUEZ, D. & THEOFILIS, V. 2010 Structural changes of laminar separation bubbles induced by global linear instability. *J. Fluid Mech.* **655**, 280–305.

SARIC, W.S., REED, H.L. & WHITE, E.B. 2003 Stability and transition of three-dimensional boundary layers. *Annu. Rev. Fluid Mech.* **35** (1), 413–440.

SAVINO, J.M. & NYLAND, T.W. 1985 Wind turbine flow visualisation studies. *Tech. Rep.* NASA Lewis Research Center.

SAXENA, V., LEIBOVICH, S. & BERKOOZ, G. 1999 Enhancement of three-dimensional instability of free shear layers. *J. Fluid Mech.* **379**, 23–38.

SCHAFFARCZYK, A.P., SCHWAB, D. & BREUER, M. 2017 Experimental detection of laminar–turbulent transition on a rotating wind turbine blade in the free atmosphere. *Wind Energy* **20**, 211–220.

SCHLATTER, P. & ÖRLÜ, R. 2012 Turbulent boundary layers at moderate Reynolds numbers: inflow length and tripping effects. *J. Fluid Mech.* **710**, 5–34.

SCHMID, P.J. & HENNINGSON, D.S. 2001 *Stability and Transition in Shear Flows*. Springer.

SCHRECK, S. & ROBINSON, M. 2002 Rotational augmentation of horizontal axis wind turbine blade aerodynamic response. *Wind Energy* **5** (2–3), 133–150.

SCHRECK, S.J., SØRENSEN, N.N. & ROBINSON, M.C. 2007 Aerodynamic structures and processes in rotationally augmented flow fields. *Wind Energy* **10** (2), 159–178.

SCHÜLEIN, E., ROSEMANN, H. & SCHABER, S. 2012 Transition detection and skin friction measurements on rotating propeller blades. In *28th Aerodynamic Measurement Technology, Ground Testing, and Flight Testing Conference*. AIAA Paper 2012-3202. AIAA.

SHEN, W.Z. & SØRENSEN, J.N. 1999 Quasi-3D Navier–Stokes model for a rotating airfoil. *J. Comput. Phys.* **150** (2), 518–548.

SICOT, C., DEVINANT, P., LOYER, S. & HUREAU, J. 2008 Rotational and turbulence effects on a wind turbine blade. Investigation of the stall mechanisms. *J. Wind Engng Ind. Aerodyn.* **96** (8–9), 1320–1331.

SWEARINGEN, J.D. & BLACKWELDER, R.F. 1987 The growth and breakdown of streamwise vortices in the presence of a wall. *J. Fluid Mech.* **182**, 255–290.

THEISS, A., HEIN, S., PASCAL, L. & CLIQUET, J. 2022 Numerical investigations of rotational effects on boundary-layer instabilities on the Z49 open rotor model. In *AIAA SCITECH 2022 Forum*. AIAA Paper 2022-2541. AIAA.

THEOFILIS, V., HEIN, S. & DALLMANN, U. 2000 On the origins of unsteadiness and three-dimensionality in a laminar separation bubble. *Phil. Trans. R. Soc. Lond.* A **358** (1777), 3229–3246.

TOOSI, S., PEPLINSKI, A., SCHLATTER, P. & VINUESA, R. 2023 The impact of finite span and wing-tip vortices on a turbulent NACA0012 wing. arXiv:2310.10857.

TOPPINGS, C. & YARUSEVYCH, S. 2023 Linear stability analysis of a three-dimensional laminar separation bubble on a finite wing. *Intl J. Heat Fluid Flow* **101**, 109141.

TRITTON, D.J. 1992 Stabilization and destabilization of turbulent shear flow in a rotating fluid. *J. Fluid Mech.* **241**, 503–523.

TRITTON, D.J. & DAVIES, P.A. 1985 Instabilities in geophysical fluid dynamics. In *Hydrodynamic Instabilities and the Transition to Turbulence*, 1st edn. (ed. H.L. Swinney & J.P. Gollub), chap. 8, pp. 229–270. Springer.

VAUGHAN, N.J. & ZAKI, T.A. 2011 Stability of zero-pressure-gradient boundary layer distorted by unsteady Klebanoff streaks. *J. Fluid Mech.* **681**, 116–153.

WALL, D.P. & NAGATA, M. 2006 Nonlinear secondary flow through a rotating channel. *J. Fluid Mech.* **564**, 25–55.

WASSERMANN, P. & KLOKER, M. 2002 Mechanisms and passive control of crossflow-vortex-induced transition in a three-dimensional boundary layer. *J. Fluid Mech.* **456**, 49–84.

WEISS, A., GARDNER, A.D., KLEIN, C. & RAFFEL, M. 2017 Boundary-layer transition measurements on Mach-scaled helicopter rotor blades in climb. *CEAS Aeronaut. J.* **8** (4), 613–623.

WEISS, A., GARDNER, A.D., SCHWERMER, T., KLEIN, C. & RAFFEL, M. 2019 On the effect of rotational forces on rotor blade boundary-layer transition. *AIAA J.* **57** (1), 252–266.

WEISS, A., WOLF, C.C., KAUFMANN, K., BRAUKMANN, J.N., HEINECK, J.T. & RAFFEL, M. 2020 Unsteady boundary-layer transition measurements and computations on a rotating blade under cyclic pitch conditions. *Exp. Fluids* **61** (2), 61.

YECKO, P. & ROSSI, M. 2004 Transient growth and instability in rotating boundary layers. *Phys. Fluids* **16** (7), 2322–2335.

YUAN, W., KHALID, M., WINDTE, J., SCHOLZ, U. & RADESPIEL, R. 2005 An investigation of low-Reynolds-number flows past airfoils. In *23rd AIAA Applied Aerodynamics Conference*. AIAA Paper 2005-4607. AIAA.

ZAKI, T.A. & DURBIN, P.A. 2005 Mode interaction and the bypass route to transition. *J. Fluid Mech.* **531**, 85–111.